

# Multi-Omic and Quantum Machine Learning Integration for Lung Subtypes Classification

Mandeep Kaur Saggi<sup>1,\*</sup>, Amandeep Singh Bhatia<sup>1,2,†</sup>, Mensah Isaiah<sup>3</sup>, Humaira Gowher<sup>3,‡</sup> and Sabre Kais<sup>2,§</sup>

<sup>1</sup> Department of Chemistry and Purdue Quantum Science and Engineering Institute, Purdue University, IN, USA

<sup>2</sup> Department of Electrical and Computer Engineering, North Carolina State University, NC, USA and

<sup>3</sup> Department of Biochemistry, Purdue University, IN, USA

Quantum Machine Learning (QML) is a red-hot field that brings novel discoveries and exciting opportunities to resolve, speed up, or refine the analysis of a wide range of computational problems. In the realm of biomedical research and personalized medicine, the significance of multi-omics integration lies in its ability to provide a thorough and holistic comprehension of complex biological systems. This technology links fundamental research to clinical practice. The insights gained from integrated omics data can be translated into clinical tools for diagnosis, prognosis, and treatment planning. The fusion of quantum computing and machine learning holds promise for unraveling complex patterns within multi-omics datasets, providing unprecedented insights into the molecular landscape of lung cancer. Due to the heterogeneity, complexity, and high dimensionality of multi-omic cancer data, characterized by the vast number of features (such as gene expression, micro-RNA, and DNA methylation) relative to the limited number of lung cancer patient samples, our prime motivation for this paper is the integration of multi-omic data, unique feature selection, and diagnostic classification of lung subtypes: lung squamous cell carcinoma (LUSC-I) and lung adenocarcinoma (LUAD-II) using quantum machine learning. We developed a method for finding best differentiating features between LUAD and LUSC datasets, which has the potential for biomarker discovery. In this paper, we show the efficacy of Quantum Neural Networks (QNNs) with three dimensions of feature encoding for the classification of multi-Omics human lung data from The Cancer Genome Atlas, comparing the framework to a variety of classical machine learning methods. Our results indicate that the Multi-omic Quantum Machine Learning Lung Subtype Classification (MQML-LungSC) framework offers superior classification performance with smaller training datasets as significant and non-significant based on p-value, thus providing compelling empirical evidence for the potential future application of unconventional computing approaches in the biomedical sciences. In comparing the performance of our proposed models based on the number of encoded features (256, 64, 32), it is evident that the model with 256 encoded features exhibits superior results across several metrics. It achieves a training accuracy of 0.95 and a testing accuracy of 0.90, which are higher than those of the models with 64 and 32 encoded features. Specifically, the model with 64 encoded features scores 0.92 for training accuracy and 0.86 for testing accuracy, while the model with 32 encoded features scores 0.88 for training accuracy and 0.85 for testing accuracy. The analyses of large-scale molecular data are beneficial for many aspects of oncology research, including the classification of possible subtypes, stages, and grades of cancer.

## I. INTRODUCTION

Quantum machine learning is pioneering a new era in computational biology, unleashing powerful tools that redefine the possibilities for tackling intricate biological challenges. The analyses of large-scale molecular data are beneficial for many aspects of oncology research, including the classification of possible subtypes, stages, and grades of cancer. Several approaches have been proposed to train networks using quantum computing technology more accurately, robustly, and efficiently [1] [2]. However, hybrid strategies have recently emerged given the current limitations of quantum machines and the constrained number of available qubits. These strategies leverage

existing technology to achieve practical and usable solutions [3]. Quantum-enhanced AI and machine learning methods are gaining attention as promising solutions to medical challenges. Recent advancements in quantum computing and quantum AI have demonstrated their wide-ranging applicability in healthcare. These methods have shown promise in various healthcare and drug-discovery domains and predicting ADME-Tox properties in drug discovery [4] [5] [6], including rapid genome analysis [7] and sequencing [8], disease detection [9], reference crop evapotranspiration classification [10], for chemistry and electronic structure calculations [11], [12] [13] [14]. Moreover, quantum computing models play a significant role in predicting gene mutations critical for the pathogenesis and diagnosis of specific cancer types, such as the Glioma Tumor Classification [15]. Cancer sub-type classification is crucial for understanding cancer pathogenesis and developing targeted treatments that can benefit patients the most [16]. Lung cancer is the most commonly diagnosed malignant tumor and is a leading cause of cancer-associated mortality. It is the second

\* drmandeepsaggi@gmail.com, msaggi@purdue.edu

† drasinghbhatia@gmail.com

‡ hgowher@purdue.edu

§ skais@ncsu.edu; Corresponding author1: skais@ncsu.edu; Corresponding author2: hgowher@purdue.edu

highest cause of new cancer cases in both genders in the United States and is the second leading cause of cancer deaths in females globally. The most common subtypes of lung cancers are lung squamous cell carcinoma (LUSC) and lung adenocarcinoma (LUAD), classified together as non-small cell lung cancer (NSCLC). The GDC-TCGA dataset provides diverse omic data crucial for cancer research and subtype classification. Specifically, for LUSC and LUAD cancer subtype the dataset includes **DNA Methylation (DNAm)**: This dataset, derived from the Illumina Human Methylation 450 platform, provides beta values indicating DNA methylation levels across various genes. This data helps identify methylation patterns that are specific to LUAD and LUSC subtypes, revealing regulatory changes associated with each cancer type (which means DNA methylation features are present (indicative of significant regulatory changes) or absent (no significant changes) in each subtype to understand their role in tumor biology). Each sample in this dataset represents tumor tissue from an individual patient, with data formatted as rows of gene identifiers and columns of sample beta values. **RNA Sequencing (RNA-seq)**: Measures gene expression levels by analyzing RNA from tumor tissues using the HTSeq platform, helping to identify genes with differential expression between LUAD and LUSC subtypes. The RNA-seq data are presented as  $\log_2(\text{count} + 1)$  values, reflecting the relative expression of genes. **MicroRNA Sequencing (miRNA-seq)**: This dataset quantifies microRNA expression levels using stem-loop expression technology. The miRNA-seq data are also transformed into  $\log_2(\text{RPM} + 1)$  values, providing insights into the regulatory roles of microRNAs in LUAD and LUSC. Each sample represents tumor tissue from an individual patient, and the data are organized into rows of miRNA identifiers and columns of expression values. For LUAD vs. LUSC subtype classification, the dataset includes primary tumor and solid tissue normal samples from which these multiomic features are derived. This approach allows for a thorough examination of molecular differences between the lung subtypes, and enhancing diagnostic accuracy.

Traditional studies often analyze individual omic features in isolation, focusing on discrete datasets such as DNA Methylation patterns [17], gene expression profiles [18], or microRNA levels. In these contexts, a "sample" refers to a biological specimen collected from a patient, such as a piece of tumor tissue or a blood sample. Each sample provides specific molecular data representing that patient's unique biological characteristics. This isolated approach, which examines data from each sample separately, can miss valuable insights from the interactions and correlations between molecular features across different samples.

In contrast, our MQML-LungSC framework integrates DNA-Methylation, RNA-seq, and miRNA-seq data to explore the interconnectedness of molecular features across a wide range of tumor samples. By examining the relationships between gene expression levels, methylation

patterns, and microRNA profiles both within individual samples and across a population of samples, we can identify complex interactions and patterns that differentiate LUAD from LUSC. This integrated analysis allows for a more comprehensive understanding of the molecular mechanisms underlying these lung subtypes, potentially leading to more accurate classification and the discovery of significant features.

In Fig. 1, the development of lung cancer is illustrated by comparing normal cells to tumor cells. However, recent studies have suggested that LUAD and LUSC should be classified and treated as different cancers [19]. Previous studies have utilized traditional feature selection and machine learning methods for cancer diagnosis, detection, and classification, but few have extended them to study potential features and biological pathways to discriminate between LUAD and LUSC [20]. To improve cancer classification accuracy, novel machine learning and feature selection methods have been developed. However, few studies have used overlapping features from different methods for classification, gene expression analysis, and molecular features [21] [22].

This work proposes a novel lung sub-type classification method that integrates classical feature selection techniques with a quantum classifier. This hybrid approach aims to enhance the accuracy and robustness of sub-type classification, thereby potentially contributing to the development of more effective cancer therapies. We propose a set of hybrid quantum computing and advanced machine learning approaches to apply machine learning on small datasets, such as (primary tumor and normal) sample types in The Cancer Genome Atlas (TCGA). These approaches aim to address the well-known "big n, small m" problem in multi-cancer analysis (Lung subtype diagnosis or classification), including (LUSC) and (LUAD).

The cancer datasets named (LUSC) and (LUAD) are taken from the Multi-Omics Cancer Benchmark TCGA (<http://cancergenome.nih.gov/>) Pre-processed Data, publicly available at the Multi-Omics Cancer Benchmark repository. For our study we employed omics datasets for transcriptome profiling by RNA-seq and miRNA-seq (micro-RNA) DNA methylation analysis by Methylation Array, , and associated clinical outcomes using associated patient information. These multi-omics data were extracted for a case study of LUSC and LUAD. To the best of our knowledge, this study is the first to utilize GDC-TCGA data within a Quantum-Classical framework using combination of omics data (DNA methylation, transcriptome profiling from RNA-seq, and miRNA-seq, and clinical outcomes) data for lung subtype classification and molecular features identification.

**Problem Formulation and Motivation:** Accurate diagnostic classification of subtypes can greatly help physicians to choose surveillance and treatment strategies for patients. Following the explosive growth of huge amounts of biological data, the shift from traditional bio-statistical methods to computer-aided means has made machine-

learning methods an integral part of today’s cancer prognosis and diagnosis. Integration of multi-omics data allows more advanced comprehensive and systematic analysis of biological changes, providing a new biomarkers for the early diagnosis of diseases. However, there are several challenges in integrating and analyzing cancer multi-omics data on a large scale. TCGA database consists of several cancer omics datasets, including transcriptome and proteome profiling, copy number variable, somatic structural, and DNA methylation. Mostly, multi-omics is characterized by high noise, high multidimensionality, and multidimensional heterogeneity, such as (big “n” and small “m”) affecting the efficiency of classification tasks, where “n” refers to the number of features/genes and “m” samples ((i) DNA: 503 samples and 485,577 genes, (ii) RNA: 585 samples and 60,488 genes, (iii) miRNA: 564 samples and 1,881 genes) for LUAD. (i) DNA: 412 samples and 485,577 genes, (ii) RNA: 550 samples and 60,488 genes, (iii) miRNA: 523 samples and 1,881 genes) for LUSC.

**Main contributions:** This study introduces a hybrid quantum classification model for distinguishing between LUSC-I tumor and LUAD-II tumor subtypes of lung datasets. In the classical section, we aim to identify the most important combination of multi-omic molecular markers using the feature selection technique. The multi-omic integrated features are encoded in the quantum section with different dimensions to find the best combination and hit list using quantum-classical model weights for tumor classification in LUAD.

To summarize, this paper makes the following contributions:

- Developed a pipeline for data pre-processing, feature engineering based on p-value t-test employs significant and non-significant using high dimensions of omic datasets which include DName, miRNA-seq and RNA-seq in LUAD and LUSC subtype dataset.
- Proposed a classical machine learning and filter methods for feature selection using random forest, mutual information, chi-square, and PCA on single omics and select top 85-85-86 features from each omic for further integration and selection of clinical attributes such as age, gender, pathological stage, survival status etc using GDC TCGA dataset.
- Developed the quantum neural network algorithm to encode the 32 features, 64 features, and 256 features with amplitude encoding for subtype-I and subtype-II classification and find the top-hit features with the qnn layer/dense layer for further visualization plots such as violin, dot plot, heatmap clustering, and PCA.
- Evaluated the accuracy and strength of the proposed quantum machine learning framework using three encoding structures of dimensions with fewer parameters and many epochs.

The remainder of the article is organized as follows. Section II presents the Materials and Methods, including the dataset, processes, and methods. Section III outlines the proposed methodology of our framework, detailing the implementation process and describing the multi-omic quantum machine learning approach. Section IV provides the results and performance analysis, including experimental results on multi-omic integrations across three dimensions, comparisons with classical classifiers, and single-omic datasets. Section V discusses the findings and outcomes. Finally, Section VI concludes the paper and explores future research directions.

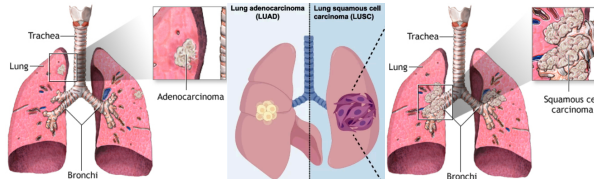
## II. MATERIAL AND METHODS

This section provides a comprehensive overview of the methods utilized in our study. We describe the feature engineering process, feature selection methods, and proposed quantum neural network model for diagnosing lung dataset subtypes LUAD and LUSC. Each subsection below elaborates on these methods in detail.

### A. Study Population

TCGA is a cancer multi-omics database generated by the National Institutes of Health Our proposed framework comprises four types of omics datasets: Gene expression, miRNA expression, DNA methylation, and Clinical patient information of lung squamous cell carcinoma. The number of samples acquired for selecting features that distinguish between LUSC and LUAD datasets is presented in Fig 1 and well detailed in Algorithm 1.

The original dataset comprised genomic data from various modalities, including DName, miRNA-seq, and RNA-seq, obtained from a cohort of patients with (LUAD) and (LUSC) lung. Specifically, the DName array dataset consisted from 503 patients with 485,577 features; the miRNA dataset contained samples from 564 patients with 1,881 features, and the RNA dataset encompassed samples from 585 patients with 60,488 features of the lung dataset. A summary of their clinical information is provided in Fig 1, with more comprehensive details available on the GDC-TCGA website. As described in Algorithm 1, We have selected three omics modalities for this study, and a summary of clinical samples is shown in Fig 1. The original dataset comprised genomic data from various modalities, including DName, miRNA-seq, and RNA-seq, obtained from a cohort of patients with (LUAD) and (LUSC) lung. Specifically, the DName array dataset consisted from 503 patients with 485,577 features; the miRNA dataset contained samples from 564 patients with 1,881 features, and the RNA dataset encompassed samples from 585 patients with 60,488 features of the lung dataset. A summary of their clinical information is provided in Fig 1, with more comprehensive details available on the GDC-TCGA web-



Diagnosis	Gender	Sample Type (Code)		
LUSC-I	Male	303	Primary Solid Tumor (01)	370
	Female	266	Solid Tissue Normal (11)	42
LUAD-II	Male	237	Primary Solid Tumor	469
	Female	109	Solid Tissue Normal	32
Combined			Recurrent Solid Tumor	2

Subtypes I and II	Age	PS	Ethnicity	Race
40-90	Stage I		Not Hispanic or Latino (640)	White (698)
	IA to IIA		Hispanic or Latino (17)	Black & African (82)
	IB to IIB		Asian (14)	Asian (14)
	IV no report		No report (258)	No report (121)

Type of Omic	Omic Field	Raw LUSC Samples	LUSC Sample	Join-DNA LUSC	Samples	Raw Features	Filter Features
DNA-Methylation	Epigenomics or Methyloomics	412 (T=370, N=42)	412	412	915	485577	396065
RNA-seq	Transcript-omics	550 (T=501, N=49)	550			60488	58327
miRNA-seq	Transcript-omics	523 (T= 477, N=46)	523			1881	1636
Type of Omic	Omic Field	Raw LUAD Samples	LUAD Sample	Join-DNA LUAD	Samples	Raw Features	Filter Features
DNA-Methylation	Epigenomics or Methyloomics	503 (T=469, N=32, R=2)	503	503	915	485577	396065
RNA-seq	Transcript-omics	585 (T=524, N=59, R=2)	585			60488	58327
miRNA-seq	Transcript-omics	564 (T= 516, N=46, R=2)	564			1881	1636

FIG. 1. **Summary of Multi-Omic Modalities and Clinical information** (a) **Development of Non-small cell lung cancer (NSCLC) lung cancer.** Overview of Non-Small Cell Lung Cancer (NSCLC) subtypes, highlighting the three main subtypes: adenocarcinoma (LUAD), squamous cell carcinoma (LUSC), and large cell carcinoma. This study focuses on two NSCLC subtypes, LUAD and LUSC. (b) Summary of Clinical information of subtypes diagnosis class with gender, sample type. Also combined subtypes patient’s age, Pathological stages, ethnicity, and race (c) information from GDC-TCGA with each entry indicating lung dataset subtype-I (LUSC) and subtype II (LUAD) 915 patient samples and high dimensional features of each omic

site. As described in Algorithm 1, We have selected three omics modalities for this study, and a summary of clinical samples is shown in Fig 1.

## B. Data Loading and Data Pre-processing

In the First phase, MQML takes any number of omic measures such as genomic, epigenomic, and transcriptomic datasets as input. Due to the inherent complexity and size of the dataset, pre-processing steps were necessary to ensure data quality and reduce computational burden. The LUAD and LUSC, Lung datasets are acquired from the Multi-Omics Cancer Benchmark GDC-TCGA Pre-processed Data, It consists of four types of omics datasets for a case study of lung squamous cell carcinoma.: RNA-seq, miRNA-seq, DName, and Clinical patient information. In the second phase, each omic has several gene features column-wise and patient samples row-wise. The raw data of each  $Omic1_{Subtype-I}$  and  $Omic1_{Subtype-II}$  is combined column-wise, with patient samples row-wise. Then, features that contain a sum of 0 are removed. To extract and select the survival/clinical attributes of both subtypes, combine the survival and clinical attributes based on sample type, i.e., diagnostic subtype-I and subtype-II.

## C. Feature Engineering

Then, the selected clinical samples of subtype-I and subtype-II are used to split each omic into two parts, i.e.,  $Omic1.1_{Subtype-I}$  and  $Omic1.2_{Subtype-II}$ . Each omic data is processed through a feature engineering process,

including a statistical t-test, to determine if there is a significant difference between the means of the two groups.

This process involves analyzing two omic data frames,  $Omic1.1_{Subtype-I}$  and  $Omic1.2_{Subtype-I}$ , to compare their mean values and compute statistical significance. First, the mean values for each column in both data frames are calculated. Then, a t-test is conducted for each column to determine the p-values, which assess the statistical significance of the differences between the two datasets. The mean values and p-values are then appended to their respective data frames. Finally, the updated data frames contain the original data mean values and p-values. This process integrates multiple omic datasets using minimum patient samples of Omic ( $Omic_1$ ,  $Omic_2$ , and  $Omic_3$ ) for the subtypes separately using a join operation. The integrated dataset combines each  $Omic1-2-3_{Subtype-I}$  and  $Omic1-2-3_{Subtype-II}$  mean values and p-values at the bottom of the row. Then, the entire dataset is sorted based on p-values for each  $Omic1-3_{Subtype-I}$  and  $Omic1-3_{Subtype-II}$  to identify the most and least significant values in the data frame. Common significance levels include  $\alpha = 0.05$  (most commonly used, indicating a 5% risk of a Type I error),  $\alpha = 0.01$  (more stringent, indicating a 1% risk), and  $\alpha = 0.10$  (less stringent, indicating a 10% risk). Then, each omic combined  $Omic1-2-3_{Subtype}$  data frame is isolated into independent  $Omic1_{Subtype}$ ,  $Omic2_{Subtype}$ , and  $Omic3_{Subtype}$  data frame datasets for data analysis steps. Finally, the prepared clinical and survival attributes are combined with each  $Omic_{Subtype}$  as shown in Fig. 2. The **t-test** is a statistical method used to determine if there is a significant difference between the means of two groups. In this context, it analyzes multi-omic data from two lung dataset subtypes, LUSC and LUAD. By calculating the

t-statistic, we can identify significant features that differentiate the two dataset subtypes. The t-statistic is calculated as:

$$t_{\text{statistic}} = \frac{\bar{X}_{\text{LUSC}} - \bar{X}_{\text{LUAD}}}{s_{\text{LUSC}} + s_{\text{LUAD}}} \quad (1)$$

where  $\bar{X}_{\text{LUSC}}$  is the mean of the LUSC group,  $\bar{X}_{\text{LUAD}}$  is the mean of the LUAD group,  $s_{\text{LUSC}}$  is the standard deviation of the LUSC group, and  $s_{\text{LUAD}}$  is the standard deviation of the LUAD group.

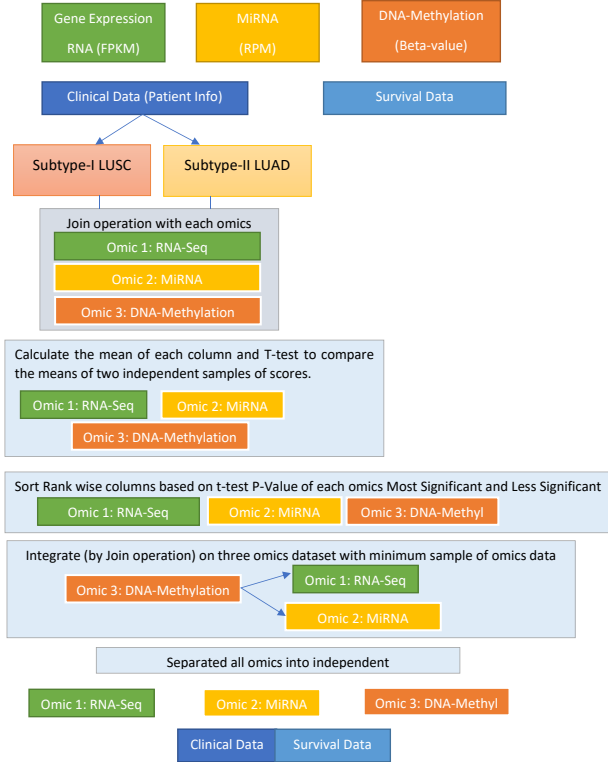


FIG. 2. **Flowchart of Data Engineering process.** This diagram illustrates the steps involved in analyzing and integrating multiple omic datasets, including mean value calculation, statistical t-tests, integration of datasets, and combination with clinical and survival attributes.

#### D. Feature Selection

In the third phase, each omic is divided into three subsets of samples:  $\text{Omic}_{S1}$ ,  $\text{Omic}_{S2}$ , and  $\text{Omic}_{S3}$ , based on p-values as shown in Table IV and Algorithm 1. We employed three steps in the feature selection process. In the first step, we determined the important features using four methods (two filter methods, one supervised method, and one unsupervised method) with the Select K Best function. Using a Venn diagram, we selected the unique features by identifying common and uncommon features. In the second step, we employed a random forest to classify the selected features from each selection

process. We then combined the features based on AUC-ROC analysis to choose the best features with an AUC greater than 0.80. In the third step, each omic's combined and reduced subset is further processed to reduce the features using hierarchical clustering based on distance.

##### 1. Feature Selection Process

In this section, we detail the feature selection process steps to identify the most relevant features for our analysis and benchmark the performance. **Model 1 Mutual Information (M33I):** measures the amount of information obtained about one random variable through another random variable. In feature selection, it quantifies the dependency between each feature and the target variable. Features with high mutual information scores are considered more informative for predicting the target variable. Equation 2 [23] defines the mutual information  $I(X_i; Y)$  as follows:

$$I(X_i; Y) = \sum_{x_i \in X_i} \sum_{y \in Y} p(x_i, y) \log \left( \frac{p(x_i, y)}{p(x_i)p(y)} \right) \quad (2)$$

where  $X_i$  is the  $i$ -th feature,  $Y$  is the target variable,  $p(x_i, y)$  is the joint probability distribution function of  $X_i$  and  $Y$ ,  $p(x_i)$  and  $p(y)$  are the marginal probability distribution functions of  $X_i$  and  $Y$ , respectively.

**Model 2 Chi-Square:** The test measures the independence between categorical variables. Feature selection quantifies the association between each categorical feature and the target variable. Features with high chi-square scores indicate a strong association with the target variable. The Chi-square value mathematical equation of joint probability genes can be calculated according to (3) [24]

$$\chi^2(X_i, Y) = \sum_{x_i \in X_i} \sum_{y \in Y} \frac{(O_{x_i, y} - E_{x_i, y})^2}{E_{x_i, y}} \quad (3)$$

where  $X_i$  is the  $i$ -th feature,  $Y$  is the target variable,  $O_{x_i, y}$  is the observed frequency of occurrence of  $X_i$  and  $Y$ , and  $E_{x_i, y}$  is the expected frequency of occurrence of  $X_i$  and  $Y$  under the null hypothesis of independence between them.

**Model 3 Random Forest Model:** is an ensemble learning method that constructs multiple decision trees during training and outputs the mode of the classes (classification) or mean prediction (regression) of the individual trees. It calculates feature importance based on how much the model's accuracy decreases when each feature is randomly shuffled. Features with higher importance scores contribute more to the predictive power of the random forest model. For classification, with the majority vote, the predicted class  $\hat{y}$  is given by [25]:

$$\hat{y} = \text{mode}(\{T_b(\mathbf{x})\}_{b=1}^B)$$

where  $B$  is the total number of trees in the forest, and  $T_b(\mathbf{x})$  is the prediction of the  $b$ -th tree for input  $\mathbf{x}$ .

**Feature Importance Calculation** in RF can be measured by evaluating how much the model’s prediction error increases when the values of a feature are permuted while keeping the other features unchanged. The feature importance for feature  $j$ ,  $FI_j$ , can be computed as:

$$FI_j = \frac{1}{B} \sum_{b=1}^B \sum_{t \in T_b} \Delta i_t \cdot 1(j \in t)$$

where:  $B$  is the total number of trees in the forest,  $T_b$  is the  $b$ -th tree,  $t$  represents a node in the tree,  $\Delta i_t$  is the decrease in impurity at node  $t$  (e.g., reduction in Gini impurity or entropy),  $1(j \in t)$  is an indicator function that is 1 if feature  $j$  is used in node  $t$ . To select the top  $k$  features based on their importance scores: (i) Compute the feature importances  $\{FI_1, FI_2, \dots, FI_p\}$ . (ii) Sort the features by their importance scores in descending order. (iii) Select the top  $k$  features with the highest importance scores.

**Model 4 Principal Component Analysis (PCA):** reduces the dimensionality of a dataset while retaining most of the variance by transforming original features into principal components [26]. The process involves standardizing the data ( $z_{ij} = \frac{x_{ij} - \mu_j}{\sigma_j}$ ), computing the covariance matrix ( $\mathbf{C} = \frac{1}{n-1} \mathbf{Z}^T \mathbf{Z}$ ), and performing eigenvalue decomposition ( $\mathbf{C} \mathbf{e}_i = \lambda_i \mathbf{e}_i$ ) to obtain eigenvalues and eigenvectors. Principal components are formed by projecting standardized data onto eigenvectors ( $\mathbf{PC} = \mathbf{Z} \mathbf{E}$ ). The top  $k$  components that explain the most variance are then selected. This transformation preserves essential data variability while reducing dimensionality.

## 2. AUC-ROC Analysis

Further, we applied the second feature selection process step to identify the best features using AUC-ROC analysis for each feature. This approach was combined with the first feature selection process, where we obtained features from RF, MI, PCA, and Chi. We set a threshold (Th) and selected features if their AUC-ROC scores for both the training and testing datasets exceeded 0.80(Th).

$$\text{Best\_features} = \{X_i \mid \text{AUC}_i^{\text{train}} > \text{Th} \wedge \text{AUC}_i^{\text{test}} > \text{Th}\}$$

$$\text{combined\_features} = \bigcup_{\text{method}} \text{best\_features}_{\text{method}}$$

$$\text{unique\_features} = \text{unique}(\text{combined\_features})$$

$$S_{\text{unique}} = \{x \mid x \in S_{\text{all}}\} \quad (4)$$

- $S_{\text{all}}$  represents the set of all selected features.

- $S_{\text{unique}}$  represents the set of selected features with duplicates removed.

The Best features are selected from different methods, combined into a single list, and remove any duplicate features from the combined list. The combined\_features denote the combined list of best features. The unique\_features denote the list of unique features after removing duplicates.

## 3. Hierarchical Clustering

Further, we have applied the third feature selection process step i.e. hierarchical clustering in two ways. Where one approach is based on the dendrogram clusters to select the best features using clusters and second approach is to compute the pairwise distance between features with distance to select the features. The approaches are: **1. Dendrogram Clusters.** Given a dataset represented by  $OMIC_{\text{Subset}1}$  to 3, where each column represents a feature, we perform hierarchical dendrogram clustering to identify clusters of similar features. We create a dendrogram from the linkage matrix  $L$  and Assign cluster IDs to the features using the function.

$$D = \text{dendrogram}(L) C_i = \text{fcluster}(L, t) \quad (5)$$

In order to extract features by each cluster, we store features in a dictionary called clusters, where each key is a cluster label  $C_i$ , and the corresponding value is a list of features belonging to that cluster. For each cluster  $C_i$ , we compute the feature importance  $I(C_i)$  by summing the absolute values of the features in the cluster.

$$I(C_i) = \sum_{f \in F(C_i)} |f| \quad (6)$$

$$\text{selected\_features\_with\_cluster} = \bigcup_i \text{Top}_K(I(C_i)) \quad (7)$$

$$\text{best\_features\_unique} = \text{set}(\text{selected\_features\_with\_cluster}) \quad (8)$$

Then, selected the top  $K$  important features from each cluster to form selected\_features\_with\_cluster and merge the selected features to get a unique set of best features.

**2. Pairwise Distances** In the second approach, the hierarchical clustering is performed on the pairwise distance matrix  $D$  using the Ward linkage method, which aims to minimize the variance when forming clusters. We compute the pairwise distance matrix  $D$  using the Euclidean metric between the transpose of the scaled feature matrix  $OMIC_{\text{SUBSET}}[S_{\text{unique}}]$ . The Euclidean distance between two points  $p$  and  $q$  in  $n$ - dimensional space and set a distance threshold  $\theta$  to a specific value i.e.  $\theta = 3.5$ . is given by:

$$\text{Euclidean distance}(p, q) = \sqrt{\sum_{i=1}^n (q_i - p_i)^2} \quad (9)$$

The Ward linkage criterion is calculated as [27]:

$$Z = \text{linkage}(D, \text{method} = 'ward')$$

$$d(u, v) = \sqrt{\frac{|v| + |s|}{|T|} d(v, s)^2 + \frac{|v| + |t|}{|T|} d(v, t)^2 - \frac{|v|}{|T|} d(s, t)^2} \quad (10)$$

where,  $d(u, v)$  represents the distance between clusters  $u$  and  $v$ , and  $|v|$ ,  $|s|$ ,  $|t|$ , and  $|T|$  denote the number of points in clusters and subclusters, and  $d(v, s)$ ,  $d(v, t)$ , and  $d(s, t)$  are the distances between clusters and subclusters.

### E. Diagnostic Classical and Quantum Classifiers

In the fourth phase, we define the machine learning and quantum machine learning methods employed for subtype-I and subtype-II lung datasets diagnostic classification. In our experimental analysis, we used four distinct machine-learning algorithms. This section comprehensively overviews these classifiers and their respective theoretical implementations.

**Logistic Regression (LR)** is a linear model used for binary classification problems. Using the logistic function, it estimates the probability that an instance belongs to a particular class. The model is based on the linear combination of input features [28].

$$\text{Logistic Function : } \sigma(z) = \frac{1}{1 + e^{-z}}$$

$$\text{Prediction: } \hat{y} = \sigma(\mathbf{w}^T \mathbf{x} + b) \quad (11)$$

$$\text{Log loss: } -\frac{1}{N} \sum_{i=1}^N [y_i \log(\hat{y}_i) + (1 - y_i) \log(1 - \hat{y}_i)]$$

Where  $\mathbf{w}$  represents the weights,  $\mathbf{x}$  the input features,  $b$  the bias term,  $\hat{y}$  the predicted probability, and  $y$  the actual label. Regularization can be applied to prevent overfitting, and in this case, L2 regularization is used with a penalty parameter  $C = 0.1$ .

**Multi-Layer Perceptron (MLP)** for a MLP with  $L$  layers, the activation  $a_j^{(l)}$  of neuron  $j$  in layer  $l$  is computed recursively from the input layer  $l = 1$  to the output layer  $l = L$  [29]:

$$a_j^{(l)} = f \left( \sum_{i=1}^{n^{(l-1)}} w_{ij}^{(l)} a_i^{(l-1)} + b_j^{(l)} \right)$$

where:  $a_j^{(l)}$ : Activation of neuron  $j$  in layer  $l$ ,  $w_{ij}^{(l)}$ : Weight connecting neuron  $i$  in layer  $l - 1$  to neuron  $j$  in layer  $l$ ,  $a_i^{(l-1)}$ : Activation of neuron  $i$  in the previous layer  $l - 1$ ,  $b_j^{(l)}$ : Bias term for neuron  $j$  in layer  $l$ ,  $f$ : Activation function applied element-wise to the linear combination.

**Support Vector Machine (SVM)** is a supervised learning model used for classification tasks. It finds the

optimal hyperplane that maximizes the margin between different classes. The kernel trick allows SVMs to perform non-linear classification by mapping input features into higher-dimensional space [30]

$$\text{Decision Function: } f(\mathbf{x}) = \mathbf{w}^T \phi(\mathbf{x}) + b$$

Optimization Problem:

$$\min_{\mathbf{w}, b} \frac{1}{2} \|\mathbf{w}\|^2 + C \sum_{i=1}^N \max(0, 1 - y_i(\mathbf{w}^T \phi(\mathbf{x}_i) + b)) \quad (12)$$

Where  $\phi$  is the feature mapping function (RBF kernel in this case),  $\mathbf{w}$  the weight vector,  $b$  the bias term,  $C$  is the regularization parameter, and  $y$  the actual label.

**Random Forest (RF)** is an ensemble learning method that constructs multiple decision trees during training and outputs the class that is the mode of the classes (classification) or mean prediction (regression) of the individual trees [25]. It is robust to over-fitting and performs well on many datasets.

$$\text{Prediction: } \hat{y} = \frac{1}{T} \sum_{t=1}^T h_t(\mathbf{x}) \quad (13)$$

Where,  $T$  is the number of trees, and  $h_t$  is the prediction of the  $t$ -th tree. Parameters such as the number of estimators (trees), criterion (e.g., entropy), max depth, and others can be tuned for optimal performance.

**Quantum Neural Network (QNN)**: In this section, we will provide an overview of the hybrid quantum neural network model, detailing the methodology used for three different models. Each model varies in the number of features (256, 64, and 32) and the corresponding number of qubits (8, 6, and 5) used for encoding, respectively. The models are named as QNN<sub>1</sub> for 256 features, QNN<sub>2</sub> for 64 features and QNN<sub>3</sub> for 32 features. The summary of hybrid models is given in Table I. The hybrid model leverages a combination of QNNs and classical neural networks (CNN).

**Feature Encoding:** The initial step involves encoding a classical vector into a quantum state. To efficiently simulate quantum circuits, each feature vector  $N$ -dimensional  $x$  is normalized and embedded into a quantum state  $|\psi\rangle$  using amplitude encoding as

$$|\psi_x\rangle = \frac{1}{\|x\|} \sum_{j=1}^N x_j |j\rangle \quad (14)$$

TABLE I. Summary of hybrid quantum-classical models

Models	Features	Qubits	Depth	Gates	Dense
QNN <sub>1</sub>	256	8	5	8 Rot, 7 CZ	256
QNN <sub>2</sub>	64	6	5	6 Rot, 5 CZ	64
QNN <sub>3</sub>	32	5	5	5 Rot, 4 CZ	32

**Quantum Layer Ansatz:** Subsequently, a sequence of parameterized quantum gates, denoted as  $U(\theta)$ , is applied to the quantum state. This unitary transformation

$U(\theta)$  consists of several local quantum gates, such as two-qubit unitaries. The entire quantum circuit  $U$  is made up of  $n$  unitary blocks, expressed as  $\mathcal{U}(\vec{\theta}) = U_1 U_2 \dots U_n$ , where  $i$ th unitary block is:

$$U_i(\theta_i) = \exp(-i\theta_i P) \quad (15)$$

where  $P$  consists of Pauli operators, and  $\theta_i$  denotes a gate parameter vector of  $U_i(\theta_i)$ .

---

**Algorithm 1** MQML-LungSC: Multi-Omic Quantum Machine Learning for Lung Subtype Classification Framework Analysis Workflow

---

1: **Input:** GDC-TCGA dataset Type: LUSC and LUAD Lung dataset, 915 patients  
2: DNA-OMIC 1: DNA<sub>S1</sub>, DNA<sub>S2</sub>, DNA<sub>S3</sub>, RNA-OMIC 2: RNA<sub>S1</sub>, RNA<sub>S2</sub>, RNA<sub>S3</sub>, miRNA-OMIC 3: miRNA<sub>S1</sub>, miRNA<sub>S2</sub>  
3: Dataset Patients: (i) DNA: 503 samples & 485,577 genes, (ii) RNA: 585 samples & 60,488 genes, (iii) miRNA: 564 samples & 1,881 genes.  
4: Feature Selection: (i) Mutual Information(MI), (ii) Chi-square, (iii) Principal Component Analysis(PCA), (iv) Random Forest(RF)  
5: Expressions:  $X'$  is the resulting matrix.  $x$  represents a row vector in  $X$ .  $x_i$  represents the  $i$ th element of the row vector  $x$ .  $n$  is the number of elements in each row vector  $x$ .  
6: **PHASE 1- Data Acquisition and Data Preprocessing:**  
7: *Multi-Omics:* (i) DNA: 503 samples & 485,577, (ii) RNA: 585 samples & 60,488 genes, (iii) miRNA: 564 samples & 1,881 genes.  
8: *Pre-processing: Combined LUAD and LUSC: Concatenate Raw Omics* OMIC-Data<sub>LUSC</sub>  $\cup$  OMIC-Data<sub>LUAD</sub>  
9: Remove rows where the sum of elements is less than or equal to 0:  $X' = \{x \in X \mid \sum_{i=1}^n x_i > 0\}$   
10: **PHASE 2- Feature Engineering: t-test Statistics**  
11: **for** Each OMIC (DNA<sub>1</sub>, RNA<sub>2</sub>, miRNA<sub>3</sub>) **do**  
12: *Combine Patient Attributes:* Combine clinical-survival patient data with OMIC[1]<sub>LUSC</sub> and OMIC[1]<sub>LUAD</sub>  
13: *Subset Splitting and Join Operation:* Rank the clinical data order based on sample sub-type and isolate LUAD and LUSC into separate data frames. Subset<sub>LUSC-I</sub>  $\cup$  Subset<sub>LUAD-II</sub>  
14: *Mean Calculation:* Calculate the mean for each column feature, i.e., column-wise genes:  $\bar{X} = \frac{1}{n} \sum_{i=1}^n X_i$   
15: *Calculate t-test:*  $t = \frac{\bar{X}_{LUSC} - \bar{X}_{LUAD}}{s_{LUSC} + s_{LUAD}}$   
16: *Sorting rank-wise features (P-value) to make significant and non-significant features*  
17: *Integrate (by join operation) with the minimum sample of omic:* Join\_Operation:(OMIC-Data<sub>1</sub>, OMIC-Data<sub>2</sub>, OMIC-Data<sub>3</sub>)  
18: *Separate all omics into independent sets of data, i.e., row-wise TCGA-ID samples and column-wise features*  
19: *Combine:* (Omic\_Dataset, Clinical\_Features, Survival\_Features) of LUAD and LUSC subtypes  
20: **end for**  
21: **PHASE 3-Feature Selection: PROCESS 1-ML methods**  
22: **for** Each OMIC (DNA<sub>LUSC-LUAD</sub>, RNA<sub>LUSC-LUAD</sub>, miRNA<sub>LUSC-LUAD</sub>) **do**  
23: Divide into subsets (Omic<sub>1</sub>: S<sub>1</sub>, S<sub>2</sub>, S<sub>3</sub>) based on the p-value and drop the features with unnamed GENE  
24: Apply the K-best selection method with a different no of features: MI, Chi, PCA, and RF on each subset.  
25: Split data into training and testing sets:  $X_{train}, X_{test}, y_{train}, y_{test} \leftarrow \text{train\_test\_split}(X_{scaled}, y_{label}, 0.2, \text{seed} = 42)$   
26: Define selected features: selected\_features  $\leftarrow$  [selected\_MI, selected\_PCA, selected\_Chi, selected\_RF]  
27: Define selected scores: selected\_scores  $\leftarrow$  [scores\_MI, scores\_PCA, scores\_Chi, scores\_RF]  
28: Initialize dictionary: best\_features  $\leftarrow$  {} and Initialize list: selected\_features\_all  $\leftarrow$  []  
29: The number of unique features and common across all the methods is given by:

$$|S_{\text{Unique}}| = |S_{\text{MI}} \cup S_{\text{PCA}} \cup S_{\text{X}^2}| - |S_{\text{Common}}|$$

$$|S_{\text{Common}}| = |S_{\text{MI}} \cap S_{\text{PCA}} \cap S_{\text{X}^2}|$$

30: **end for**

---



---

**Algorithm 2** MQML-LungSC: (Contd.)

---

1: **PROCESS 2- Perform AUC-ROC analysis with RF classifier:** Apply RF classifier (n-estimator=250) with conditions on each feature to obtain the best features.  
2: **for**  $i$  in {0, 1, 2, 3} **do**  
3: Get method, features, and scores: *method, features, scores*  $\leftarrow$  methods[ $i$ ], best\_selected\_features[ $i$ ], selected\_scores[ $i$ ]  
4: Sort features by scores  
5: **for** each feature in sorted features **do**  
6: Evaluate ROC AUC for feature of TR and TS  
7: **if** ROC AUC > 0.80 **then**  
8: Append feature to best\_selected\_features[method]  
9: **end if**  
10: **end for**  
11: **end for**  
12: Calculate total count of features, Combine best features and Remove duplicate features.  
13: **PROCESS 3- Hierarchical Clustering Selection:**  
14: (1) pairwise\_distances  $\leftarrow$  pdist( $X^T$ , metric = 'euclidean') and distance.threshold = Max\_number  
15: (2)  $Z \leftarrow$  linkage(pairwise\_distances, method = 'ward')  
16: (3) cluster  $\leftarrow$  fcluster( $Z$ , t = distance\_threshold, criterion = 'maxclust')  
17: (4) Split Cluster Group:(i)No. of clusters, (ii)Select top clusters  
18: (5) Apply heatmap and dendrogram analysis for clustering  
19: **PROCESS 4- Apply UMAP for Dimensionality Reduction:**  
20:  $X_{\text{reduced}} \leftarrow$  UMAP(n\_components = 2, min\_dist = 0.1, n\_neighbors = 15)  
21: **PROCESS 5- Apply Quantum Machine Learning:** Train the QML model on the selected features for subtype classification and calculate accuracy metrics.

---

In quantum ansatz, we have applied parameterized rotations  $R(\theta, \phi, \lambda)$ , and Controlled-Z (CZ) gates for entanglement between adjacent qubits. Each qubit undergoes a rotation defined by three parameters,  $\theta$ ,  $\phi$ , and  $\lambda$ . The rotation operation  $R(\theta, \phi, \lambda)$  can be expressed as:

$$R(\theta, \phi, \lambda) = R_z(\lambda)R_y(\theta)R_z(\phi) \quad (16)$$

The controlled-Z gates introduce entanglement between adjacent qubits, which a phase flip if both qubits are in the  $|1\rangle$  state. For instance, a single layer of ansatz applies the following unitary transformation on the 8-qubit system as:

$$U(W) = \prod_{i=0}^7 R(\theta_i, \phi_i, \lambda_i) \prod_{i=0}^6 CZ_{i,i+1} \quad (17)$$

**Measurement:** Finally, a quantum measurement ( $\hat{O}$ ) is applied using the expectation value of the Pauli-Z operator for each qubit

$$\tilde{y}_i = \langle \psi_i | \mathcal{U}(\theta)^\dagger \hat{O} \mathcal{U}(\theta) | \psi_i \rangle \quad (18)$$

The measurement results from the quantum circuit are then fed into a layer of a classical neural network, which is used to predict the label of the input state. **Objective Function:** In diagnostic classification, a binary classification task distinguishing between Subtype-I and Subtype-II using multi-omic data aims to minimize the binary cross-entropy loss. The binary cross-entropy loss function is defined as follows:

$$\mathcal{L} = -\frac{1}{N} \sum_{i=1}^N [y_i \log(\hat{y}_i) + (1 - y_i) \log(1 - \hat{y}_i)] \quad (19)$$

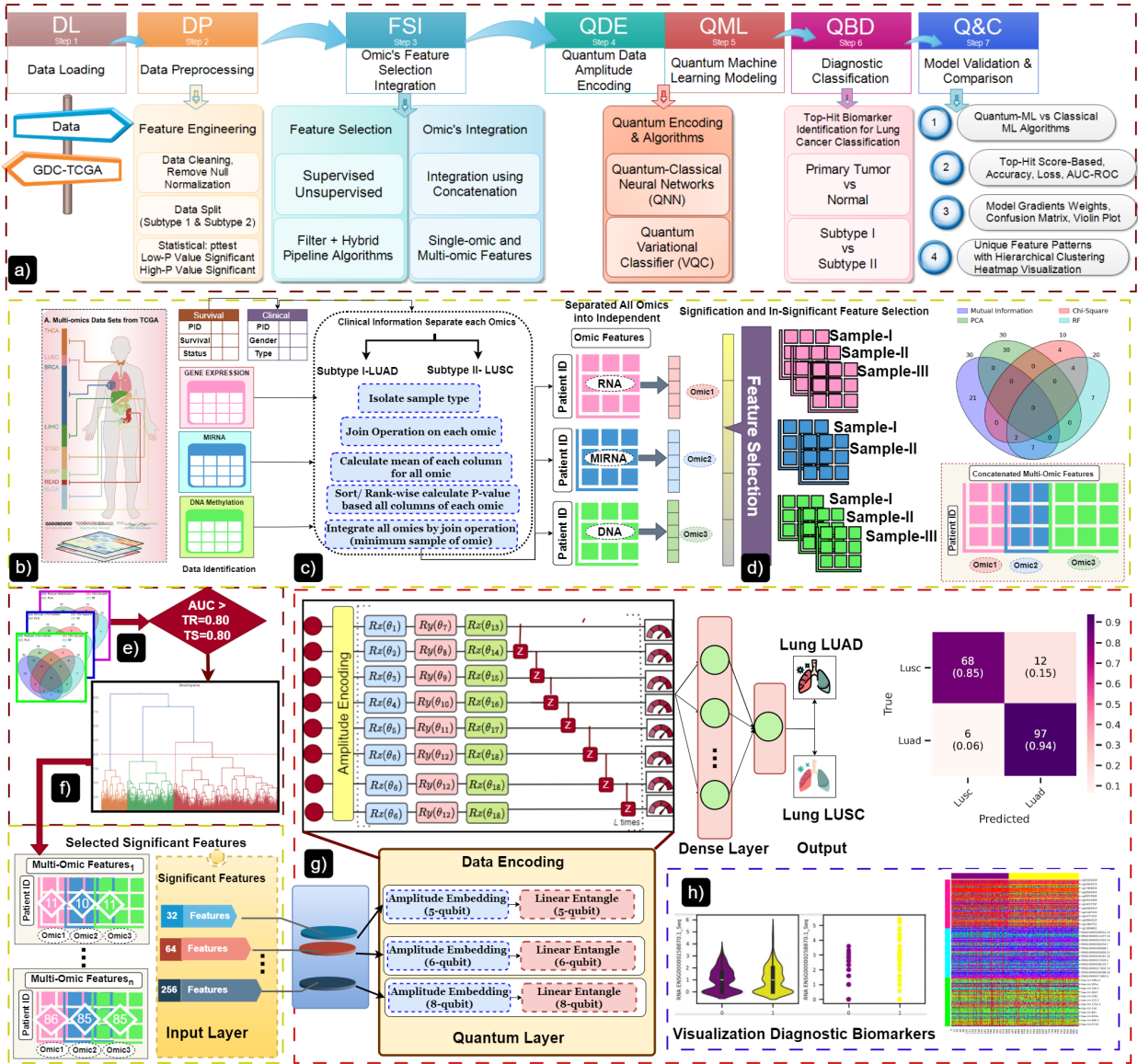


FIG. 3. Workflow of multi-omics integration and classification using quantum neural networks. (a) Schematic representation of the overall pipeline of MQML-QNN framework. (b) Data acquisition from GDC-TCGA, including (i) DName, (ii) RNA-seq, (iii) miRNA-seq, and (iv) clinical and survival attributes of patients. (c) Data preprocessing and feature engineering using t-test p-values for each omic data type to differentiate between subtypes I and II. (d)-(e) Feature selection process involving: (i) Four feature selection models: Random Forest (RF), Mutual Information (MI), Principal Component Analysis (PCA), and Chi-Squared (Chi). (ii) AUC-ROC analysis with thresholding for feature selection. (iii) Hierarchical clustering based on sample vs. feature and pairwise feature similarity using distance metrics. (f) Integration of multi-omic data resulting in 256 features from 915 common patients. (g) Quantum amplitude encoding with three feature dimensions: 32, 64, and 256, and the quantum circuit with a dense layer for diagnostic classification of LUAD versus LUSC lung datasets. (h) Visualization of features through violin plots, confusion matrices, and heatmaps.

where  $N$  is the number of samples (915 in our case),  $y_i$  is the true label for the  $i$ -th sample ( $y_i \in \{0, 1\}$ ) with (0) representing  $LUSC_{Subtype-I}$  and (1) representing  $LUAD_{Subtype-II}$ , and  $\hat{y}_i$  is the predicted probability for the  $i$ -th sample.

## F. Multi-Omic Integration and Development

In the last phase, the subsets of  $Omic_{S1}$ ,  $Omic_{S2}$ , and  $Omic_{S3}$  are combined. The multi-omic integration process is then followed to integrate all the Omic data to train the quantum neural network model using different feature dimensions with amplitude encoding, such as  $Multi-Omic_{256}$ ,  $Multi-Omic_{64}$ , and  $Multi-Omic_{32}$ .

TABLE II. Range of p-values used for selecting most significant and less significant features.

Set	OMIC1: DNAm		OMIC2: RNA-seq		OMIC3: miRNA-seq	
	P-value	Index	P-value	Index	P-value	Index
1	8.42e-25 to 4.99e-02	140000 - 299885	5.19e-24 to 4.99e-02	7000 - 36900	1.17e-25 to 4.99e-02	100-821
2	2.89e-06 to 4.99e-02	241000 - 299885	2.53e-05 to 4.99e-02	22300 - 36900	2.35e-03 to 9.93e-01	600-1586
3	4.99e-02 to 9.99e-01	299885 - 344344	4.99e-02 to 9.99e-01	36900 - 58324	-	-

TABLE III. Feature Selection Process using P-value based data

Set	OMIC1: DNA			OMIC2: RNA			OMIC3: miRNA		
	Features	FS Methods	FS Clt	Features	FS Methods	FS Clt	Features	FS Methods	FS Clt
1	159885	40	10	29900	39 (37)	20	721	70(63)	35
2	44459	70 (68)	50	14600	58 (51)	32	986	76 (63)	50
3	58885	47 (46)	25	21424	97(71)	34	-	-	-

### III. METHODOLOGY

#### A. Overview of MQML framework

We present a pioneering framework of multi-omic-quantum machine learning (MQML-LungSC) tailored for integrating data, selecting unique features, classifying diagnostics, and identifying features associated with two distinct subtypes of lung datasets: LUSC primary tumor type-I and LUAD primary tumor type-II. Due to the datasets' inherent heterogeneity, complexity, and high dimensionality, our study aims to assess the efficacy of hybrid-QML in selecting, reducing, encoding features, and classifying diagnostics between subtype-I and subtype-II patients across integrated multi-omic subtype datasets. The whole process is divided into a few phases as described in Fig 3. (i) Data loading, (ii) Data Pre-processing- Feature engineering, (iii) Feature Selection-split into three steps, (iv) quantum data encoding and circuit, (v) quantum-classical hybrid model development phase, testing phase and (vi) identification of molecular top-hit features genes. MQML processes various omic datasets (epigenomic and transcriptomic) by pre-processing to ensure data quality and reduce the computational burden. Omic features are columns, and patient samples are rows. In the first data pre-processing phase, (Omic[1]<sub>Subtype-I</sub> and Omic[1]<sub>Subtype-II</sub>) are combined and patient survival and clinical attributes are extracted based on the diagnostic subtype i.e. sample-type. In the second phase, we conducted a feature engineering process using the statistical t-test method to identify significant and non-significant features within each omic. Then, we split each Omic[1]<sub>subset1</sub> to Omic[1]<sub>subset3</sub> subset into three parts based on p-values: two subsets with p-values less than 0.05 and one subset with p-values greater than 0.05. Table IV shows the features selected using a feature selection process based on p-value for further diagnostic classification in multi-omic modalities. In the third phase, we applied a feature selection process on each Omic[1]<sub>subset1-3</sub> into three steps: (i) four machine learning feature selection methods, (ii) AUC-ROC analysis, and (iii) hierarchical clustering with distance-based

methods to obtain the most optimal and unique features for each omic subset.

In the first selection, we applied four feature selection methods: (MI), Chi-square, (PCA), and (RF). Each subset of omics/modality was then analyzed to select the best features using the four selection methods, considering both common and uncommon features. In the second step of feature selection, the total selected features were further processed based on a random forest classifier, considering only features with AUC-ROC scores higher than 0.80 in both training and testing datasets for further analysis. In the third step, then we applied the hierarchical clustering approach, selecting additional features based on two criteria: (i) Pearson-Euclidean distance between features and (ii) Euclidean distance using the ward method of clustering. The top cluster features were obtained on each Omic<sub>Subset</sub>. Finally, the selected features based on distances were processed to visualize each modality heatmap and other visualization plots. Further, this feature selection process was applied to select the best and unique features from each omic modality (DNA-me, RNA-Seq, miRNA-Seq) based on their subsets. Then, each subset of modality was combined among single omic, such as three subsets for Omic<sub>DNA-Single</sub> and Omic<sub>RNA-Single</sub>, and two subsets for Omic<sub>miRNA-Single</sub>. Further,

TABLE IV. List of P-value Based Conducted Encoding and Simulations

Set	P-value	DNAm	RNA-seq	miRNA-seq
S <sub>1</sub>	< 0.05	10	20	35
S <sub>2</sub>	< 0.05	25	32	-
S <sub>3</sub>	> 0.05	50	34	-
S <sub>4</sub>	< 0.05	-	-	51
<b>Multi-Omic Data</b>		85	86	85

in the third phase, the multi-omic integration process is followed to combine each subset of Omic1 = Omic[1]<sub>subset1</sub>+Omic[1]<sub>subset2</sub>+Omic[1]<sub>subset3</sub> and then integrate all the single Omic such as Omic<sub>1</sub>, Omic<sub>2</sub>, and Omic<sub>3</sub> to train the QNN model using different dimensions of features with amplitude encoding such as (Multi-Omic<sub>256</sub>, Multi-Omic<sub>64</sub> and Multi-Omic<sub>32</sub>). In this step, all the single omics were integrated using hierarchical

integration column-wise among 915 patient samples of LUAD and LUSC. This combined integrated dataset consists of 85 features for  $\text{Omic}_{DNA}$ , 86 for  $\text{Omic}_{RNA}$ , and 85 for  $\text{Omic}_{miRNA}$ , totaling 256 features for multi-omic analysis. Now, to evaluate the performance of the quantum model, we evaluate three QNN models on three sets of datasets. We randomly selected features to create datasets with 32 and 64 features, forming integrated multi-omic data. This allowed us to perform the QNN model classification across three data dimensions: 32, 64, and 256.

In the Fourth Phase, we developed a MQML-QNN model for the diagnostic classification of lung subtype-I and subtype-II. We compared the quantum model with classical machine learning classifiers to evaluate the performance as depicted in Table X (LR, MLP, and SVM). We benchmarked the performance of the best results with Quantum neural network and Random Forest and evaluated the comparison with all existing classical models for the 256, 64, and 32 features of integrated multi-omics as shown in Table X and Figure 13.

Additionally, In the last phase, we extracted top-hit multi-omic molecular features' importance features using the QNN model weights for further analysis. The workflow of the proposed (MQML-LungSC) framework is shown in Fig. 3.

#### IV. RESULTS AND PERFORMANCE

In this section, we will present the performance of our proposal MQML-LungSC framework in detail. The performance of MQML was designed to compare with three dimensions of QNN models that perform diagnostic subtype classification. The metrics used to compare the classification performance of (MQML-LungSC) were accuracy (ACC), loss, precision, recall, and F1-score (F1). The F1 score was calculated by the mean F1 score of each class, weighted by the size of that class. Diagnostic and Identification of LUSC and LUAD subtypes related gene after the omic data integration. For each dataset subtype, RNA-seq, DNAME and miRNA-seq are used for data integration with common patients.

##### A. Experimental Hardware and Software

We implemented the experiments on the Gilbreth GPU cluster at Purdue University's Research Computing and Data Systems (RCAC) with a single server, one GPU node, 8 cores per node, an A10 GPU, and 512 GB memory per node [31]. The experiments were performed using TensorFlow 2.7.0 in Python 2.8.0. The quantum machine learning library PennyLane (version 0.28.0) by Xanadu Inc. was employed, with dependencies including appdirs, autograd, autoray, cachetools, networkx, numpy, pennylane-lightning, requests, retworkx, scipy, semantic-version, and toml. Additionally, the fundamental array

computing package NumPy (version 1.20.3), the Python plotting package Matplotlib (version 3.4.3), the machine learning and data mining library scikit-learn (version 1.4.2), the statistical data visualization library Seaborn (version 0.11.2), and the data analysis package pandas (version 1.3.4) were utilized in the study.

##### B. Performance of Feature Engineering Process

Statistical analyses were conducted using a t-test to calculate the p-value significant and in-significant values for LUSC and LUAD subtypes. Then, each modality was divided into subsets, meaning features were divided into subsets column-wise based on the obtained p-values. For high-dimensional features in DNAME and RNA-seq modalities, the datasets were divided into three subsets based on the significance level: two subsets with p-values less than 0.05 and one subset with p-values greater than 0.05. However, the miRNA-seq modality was divided into two subsets: one included p-values less than 0.05 and the second subset had p-values greater than 0.05 to 0.9. The process of data engineering is shown in Fig 2. Table II depicts the range of p-values used for selecting the most significant and least significant features across three omics. Table III presents the feature selection process using p-value-based data across DNAME (OMIC1), RNA-seq (OMIC2), and miRNA-seq (OMIC3) omics, detailing the number of features selected, feature selection methods employed, and significance thresholds (Feature cluster) (FS Clt). Table IV provides a summary of p-value-based encoding and simulations conducted across different omic sets: DNAME, RNA-seq, and miRNA-seq. Each set (denoted as  $S_1$ ,  $S_2$ ,  $S_3$ , and  $S_4$ ) shows the threshold p-value used for feature selection and the corresponding number of features selected for each omic type. The table also includes aggregated results for multi-omic data integration, highlighting the total number of features retained across all omics.

##### C. Performance of Feature Selection Process with RF Classifier

Further, this process is applied to discover the best and unique features from each omic modality (DNAME, RNA-seq, and miRNA-seq) based on their subsets. The applied feature selection process based on p-value, the  $\text{OMIC}_{DNAME}$ ,  $\text{OMIC}_{RNA-seq}$ , and  $\text{OMIC}_{miRNA-seq}$  was divided into three subsets. The initial two subsets represent less than 0.05 and the third subset represents a greater than 0.05 p-value. The four machine learning models are applied to select the features. (DNAME subset combined Total 85=  $\text{DNAME}_{Subset1}(10) + \text{DNAME}_{Subset2}(50) + \text{DNAME}_{Subset3}(25)$  features are combined to concatenate the final subset of  $\text{OMIC}_{DNAME}$ .

RNA subset combined Total 85=  $\text{RNA-seq}_{Subset1}(20) + \text{RNA-seq}_{Subset2}(32) + \text{RNA-seq}_{Subset3}(34)$  features

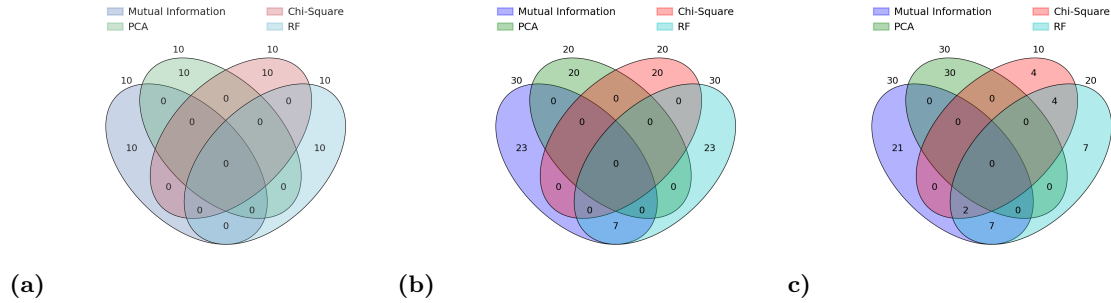


FIG. 4. **Visualization of Venn Diagram and Represents the Feature Importance Plot with score** Represent the visualization through venn diagram for the features selection process using four machine learning methods on DNA methylation (DNAm), RNA transcript level (RNA-seq), and miRNA-seq levels (miRNA) modalities. (a) DNA Sample<sub>1</sub> to Sample<sub>3</sub>, (b) RNA Sample<sub>1</sub> to Sample<sub>3</sub> and (c) miRNA Sample<sub>1</sub> to Sample<sub>2</sub>, Visualization of feature selection using four models i.e. i) Mutual information, (ii) Chi-square, (iii) Principal component (iv) Random forest of three modalities (d) DNA S<sub>1</sub> to S<sub>3</sub>, (e) RNA S<sub>1</sub> to S<sub>3</sub>, and (f) miRNA S<sub>1</sub> to S<sub>2</sub>

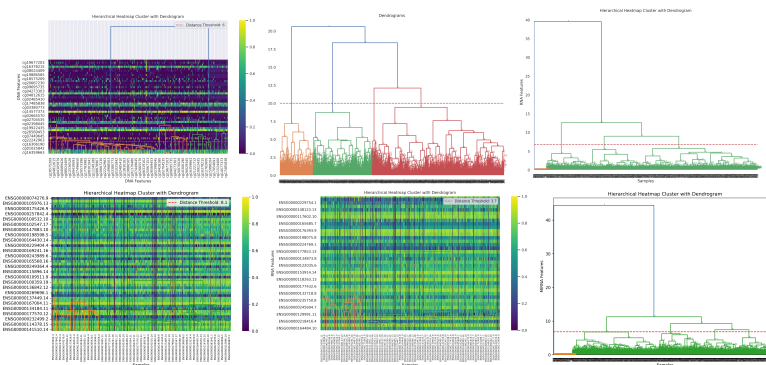


FIG. 5. **Represents the Hierarchical Clustering Dendrogram based pairwise feature selection and distance-based selection of features of each omic subsets based on (a)-(c) DNA S<sub>1</sub> to S<sub>3</sub>, (d)-(f) RNA S<sub>1</sub> to S<sub>3</sub>, and (g)-(h) miRNA S<sub>1</sub> to S<sub>3</sub>,**

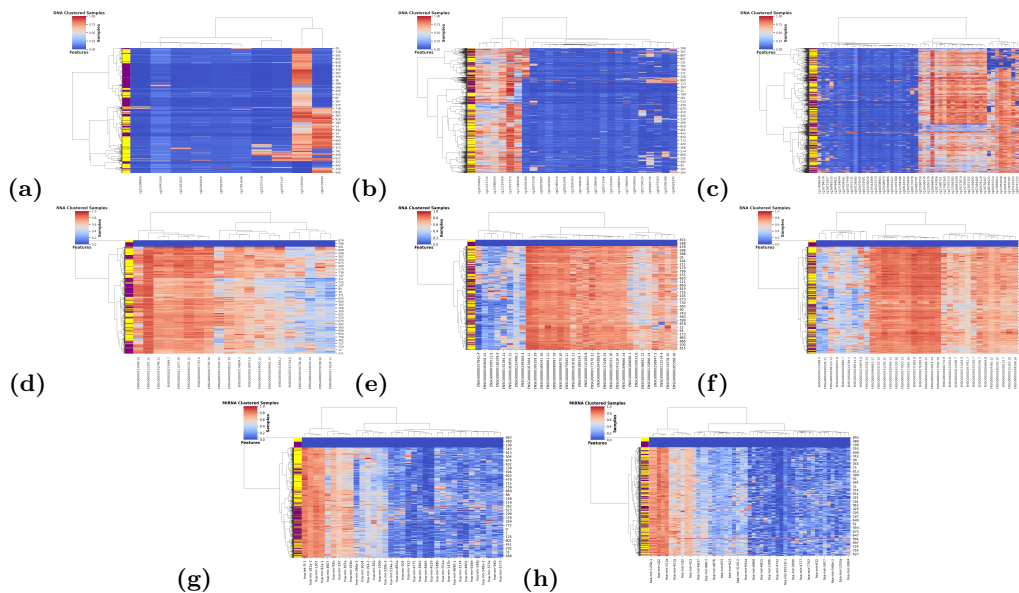


FIG. 6. **Represents the Hierarchical Clustering Heatmap of selected features of each omic subsets (a)-(c) DNA S<sub>1</sub> to S<sub>3</sub>, (d)-(f) RNA S<sub>1</sub> to S<sub>3</sub>, and (g)-(h) miRNA S<sub>1</sub> to S<sub>3</sub>,**

are combined to concatenate the final subset of  $OMIC_{RNA}$ . miRNA-seq subset combined Total 85=

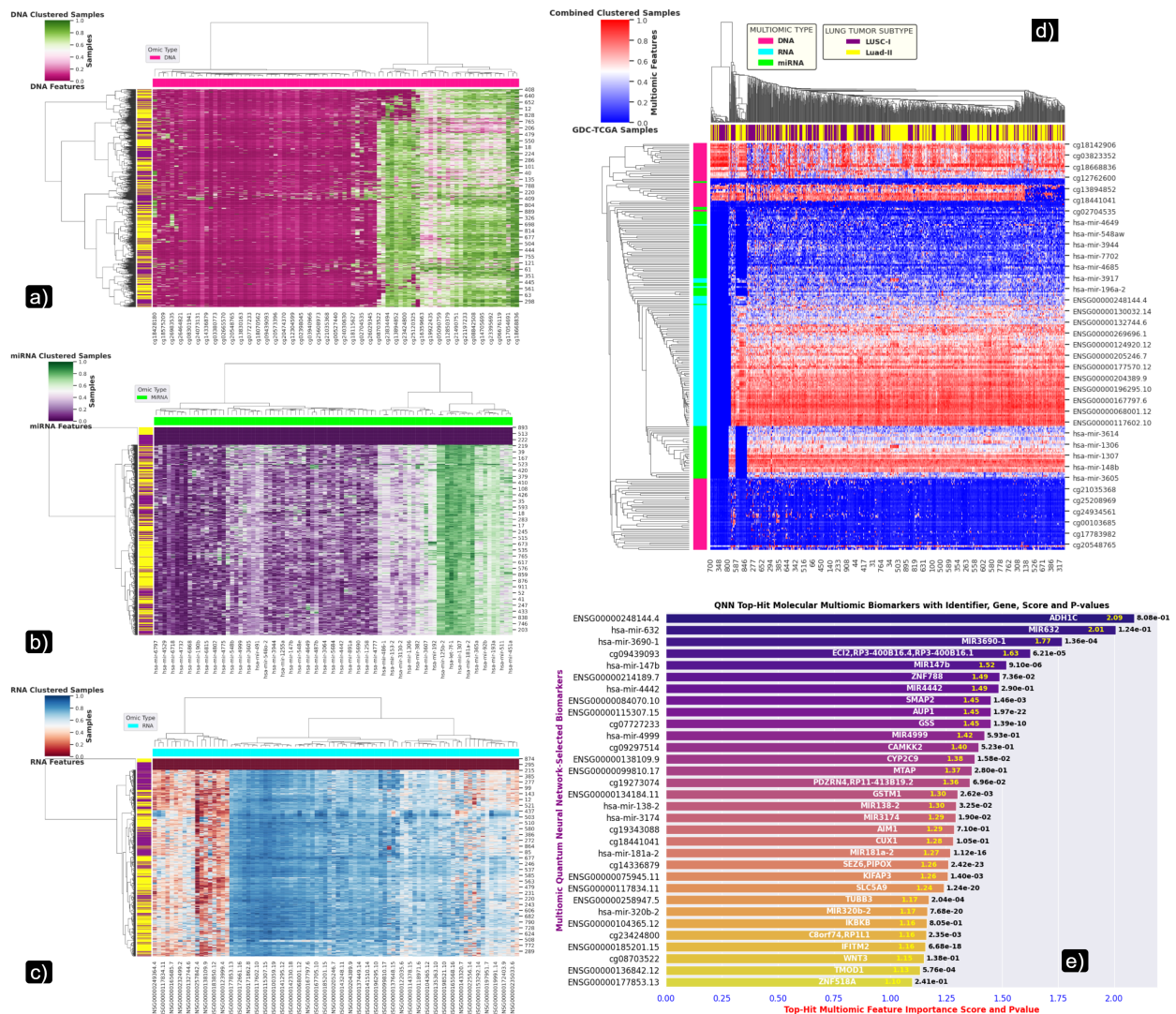


FIG. 7. Hierarchical representation of single omics and integrated multi-omic hierarchical clustering analyses and top-hit feature importance plot. Hierarchical clustering of emerging data results in the effective separation of patients’ groups. (A), whereas for DName (B) miRNA-seq (C) RNA-seq data and (D) Integrated all omics as Multi-Omic<sub>256</sub>. Heatmaps illustrate DNA methylation, gene expression, miRNA, and patterns of lung feature specific-related genes in the LUAD subtype-II compared to the LUSC subtype-I lung dataset. In each heatmap, the cell lines were organized by hierarchical clustering, with labels colored in purple (subtype-I) and yellow for (subtype-II) highlighting LUSC and LUAD patients, respectively. (E) Outcome of top molecular features of integrated multi-omic<sub>256</sub> using the QNN<sub>1256</sub> model

miRNA-seq<sub>Subset1</sub>(35) + miRNA-seq<sub>Subset2</sub>(51) features are combined to concatenate the final subset of OMIC<sub>miRNA</sub>. These four methods were used to select the features and then classified with a random forest classifier to see the performance of selected features by each method as shown in Table V. This table presents the performance metrics (Accuracy, Precision, Recall, and F1-Score) of four feature selection models—MI, PCA, Chi-sq, and RF—applied to different subsets of DName, RNA-seq, and miRNA-seq data. The Random Forest (RF) model consistently shows the highest performance across most subsets, particularly in DNA, where it nearly achieves perfect scores. MI demonstrates competitive

performance across all omics data types and subsets, especially in re-call and F1-Score. Chi-sq generally performs moderately well, while PCA tends to have the lowest performance across the board.

#### D. Performance of Multi-Omic (DName/RNA-seq/miRNA-seq) Integration of Subtype-I and Subtype-II with MQML-QNN

In this MQML-LungSC QNN framework, we integrated multi-omic DNA-seq/RNA-seq/miRNA-seq cohorts for lung subtype-I and subtype-II diagnostic clas-

TABLE V. Performance Comparison of Different Feature Selection Methods Across Omics Data Types and Subsets with RF Classifier

DName-Subset1				RNA-seq-Subset1				miRNA-seq-Subset1				
Subset1	MI	PCA	Chi-sq	RF	MI	PCA	Chi-sq	RF	MI	PCA	Chi-sq	RF
ACC	0.99	0.841	0.968	0.998	0.9	0.75	0.79	0.84	0.84	0.77	0.76	0.87
Precision	1.99	0.843	0.9677	0.99	0.91	0.75	0.76	0.84	0.88	0.79	0.77	0.9
Recall	2.99	0.874	0.97	0.998	0.916	0.82	0.89	0.86	0.82	0.8	0.81	0.86
F1-Score	3.99	0.857	0.97	0.99	0.91	0.78	0.82	0.85	0.85	0.79	0.79	0.88
DName-Subset2				RNA-seq-Subset2				miRNA-seq-Subset2				
Subset2	MI	PCA	Chi-sq	RF	MI	PCA	Chi-sq	RF	MI	PCA	Chi-sq	RF
ACC	0.998	0.75	0.94	0.99	0.85	0.78	0.69	0.88	0.77	0.66	0.63	0.8
Precision	0.99	0.76	0.95	0.99	0.86	0.7	0.73	0.89	0.79	0.68	0.61	0.81
Recall	0.99	0.8	0.93	0.998	0.88	0.78	0.71	0.91	0.78	0.72	0.88	0.82
F1-Score	0.99	0.78	0.94	0.99	0.87	0.74	0.72	0.9	0.79	0.7	0.72	0.81
DName-Subset3				RNA-seq-Subset3								
Subset3	MI	PCA	Chi-sq	RF	MI	PCA	Chi-sq	RF				
ACC	0.996	0.881	0.942	0.995	0.79	0.68	0.56	0.85	-	-	-	-
Precision	0.997	0.879	0.952	0.996	0.78	0.66	0.55	0.85	-	-	-	-
Recall	0.995	0.908	0.942	0.996	0.87	0.84	0.99	0.88	-	-	-	-
F1-Score	0.996	0.893	0.947	0.996	0.82	0.74	0.71	0.87	-	-	-	-

sification with three different dimensions of features and  $n$  qubits encoding. The QNN models are named QNN<sub>1</sub>, QNN<sub>2</sub> and QNN<sub>3</sub> based on different settings and hyperparameters as shown in Table I.

Among these models, in the QNN<sub>1256</sub> model, we have used qubit<sub>8</sub> to encode 256 features using amplitude encoding. Then, a layer is repeated consisting of single-qubit gates (Rz, Ry, Rz) Parameterized rotations 8

$$R(\theta, \phi, \lambda) = R_z(\lambda)R_y(\theta)R_z(\phi)$$

on each qubit, followed by a linear entanglement of 7 Controlled-Z (CZ) gates between adjacent qubits. Finally, the measurement is performed on all qubits, followed by classical neurons and a dense layer for the classification using ADAM optimizer. This QNN<sub>1256</sub> model, provided the highest classification performance, with an accuracy score of 0.90. In this model, for the LUAD<sub>Subtype-II</sub> class, the precision, recall, and F1 scores were 0.89, 0.94, and 0.92, respectively, whereas for the LUSC<sub>Subtype-I</sub> class, the precision, recall, and F1 score were 0.92, 0.85, and 0.88 respectively for the testing multi-omic dataset.

TABLE VI. Performance of QNN models on differentiating LUAD vs LUSC with different number of features.

Models	QNN-256		QNN-64		QNN-32	
	LUSC	LUAD	LUSC	LUAD	LUSC	LUAD
Precision	0.92	0.89	0.85	0.86	0.83	0.88
Recall	0.85	0.94	0.81	0.89	0.85	0.87
F1-Score	0.88	0.92	0.83	0.88	0.84	0.87
Class	80	103	79	104	79	104
Accuracy	0.9	0.9	0.86	0.86	0.85	0.85

The QNN<sub>264</sub> model demonstrated secondary predictive performance with an accuracy of 0.86. In the QNN<sub>264</sub> model circuit, qubit<sub>6</sub> used to encode 64 features with amplitude encoding are employed within the feature map and apply 6 rotation gates with 5 CZ gates and a classical dense layer. In the context of the QNN<sub>264</sub> model, the precision, recall, and F1 score values for the LUAD<sub>Subtype-II</sub> class were 0.86, 0.89, and 0.88, respectively. In contrast, for the LUSC<sub>Subtype-I</sub> class, the cor-

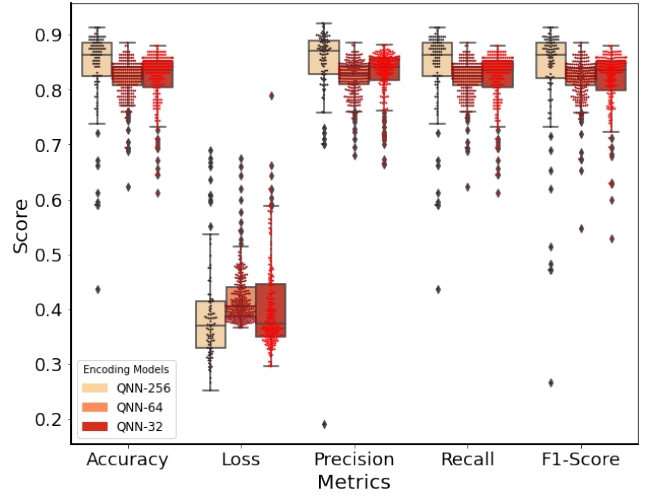


FIG. 8. Comparison of QNN models with different encoding features on integrated multi-omic data based on different classification metrics.

responding precision, recall, and F1 scores are 0.85, 0.81, and 0.83, respectively.

Similarly, the QNN<sub>332</sub> model exhibited improved performance with an accuracy of 0.85. In the QNN<sub>332</sub> model circuit qubit<sub>5</sub> is used to encode 32 features with amplitude encoding and apply 5 rotation gates with 4 CZ gates using a classical dense layer. In the context of the QNN<sub>332</sub> model, the precision, recall, and F1 score values for the LUAD<sub>Subtype-II</sub> class were 0.88, 0.87, and 0.87 respectively. In contrast, for the LUSC<sub>Subtype-I</sub> class, the corresponding values for precision, recall, and F1 score are 0.83, 0.85, and 0.84 respectively.

Each subset of modality was combined to make a feature of the Multi-Omic dataset (DNA subset combined Total 85= DName<sub>Subset1</sub>(10) +DName<sub>Subset2</sub>(50) + DName<sub>Subset3</sub>(25), RNA-seq subset combined 86= RNA-seq<sub>Subset1</sub>(20) + RNA-seq<sub>Subset2</sub>(32) + RNA-seq<sub>Subset3</sub>(34) and (miRNA-seq subset combined total = 85 miRNA-seq<sub>Subset1</sub>(35) + miRNA-seq<sub>Subset2</sub>(51).

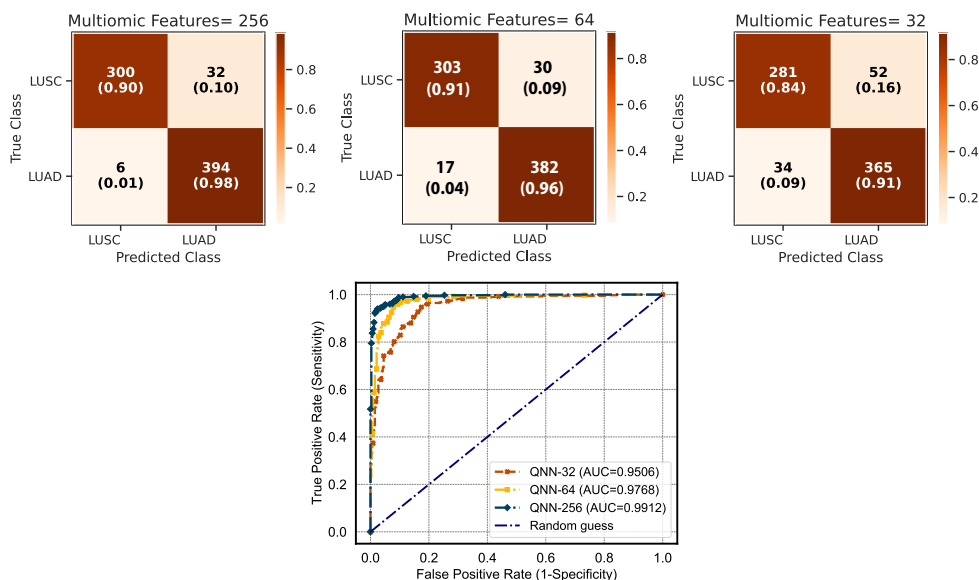


FIG. 9. Represents the performance of QNN model on (a) 256, (b) 64, (c) 32 features, (d) AUC-ROC on the training dataset respectively Visualization of Confusion Matrix on training dataset respectively

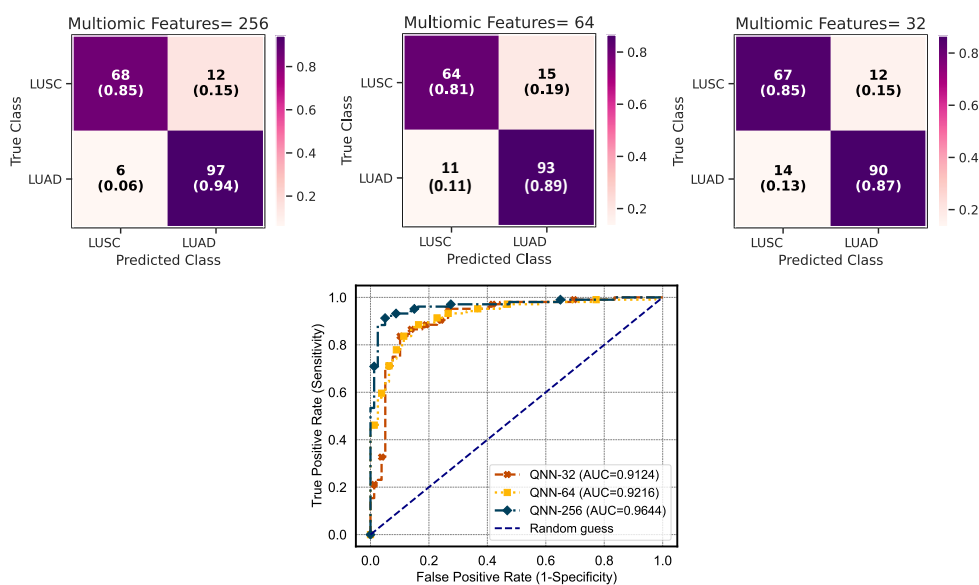


FIG. 10. Represents the performance of QNN model on (a) 256, (b) 64, (c) 32 features (d) AUC-ROC on testing dataset respectively Visualization of Confusion Matrix on testing dataset respectively

Thus, the integration of three types of molecular data (RNA-seq, DNAm, and miRNA-seq) can achieve better results for the patients' subtype-prediction. MQML-LungSC achieves superior performance when integrating a variable number of modalities while including a smaller number of samples. Our results indicate that the Multi-Omic Quantum Machine Learning Lung Subtype Classification (MQML-LungSC) framework offers superior classification performance with smaller training datasets as significant and non-significant based on p-value, thus providing compelling empirical evidence for the potential fu-

ture application of unconventional computing approaches in the biomedical sciences. We observed that as we increased the number of features, we achieved superior performance in diagnostic classification and improved significance in distinguishing between significant and non-significant p-subtypes. Additionally, we identified the best features within the 32 and 64-feature datasets to highlight the top-hit multi-omic features for further investigations. Fig 7. presents the hierarchical representation and clustering analysis of single omics and integrated multi-omic data. Heatmaps illustrate DNAm, RNA-seq,

TABLE VII. Top 40 features identified by the QNN<sub>256</sub> model, including their gene names, P-values, feature importance (FI), Feature-specific based on their mean levels in LUAD and LUSC (i.e. Luad-Tumor, Luad-Normal, Lusc-Tumor and Lusc-Normal)

Features	P-values	FI	Gene	Feat. Specific
ENSG00000248144.4	0.8082	2.08	ADH1C	LUSC Normal
hsa-mir-632	0.1245	2.007	MIR632	LUAD Tumor
hsa-mir-3690-1	0.00013	1.768	MIR3690-1	LUSC Normal
cg09439093	6.21E-05	1.625	ECI2,	LUAD Tumor
hsa-mir-147b	9.10E-06	1.518	MIR147b	LUAD Tumor
ENSG00000214189.7	0.0736	1.487	ZNF788	LUSC Normal
hsa-mir-4442	0.2897	1.485	MIR4442	LUAD Tumor
ENSG00000084070.10	0.0014	1.450	SMAP2	LUSC Normal
ENSG00000115307.15	1.97E-22	1.449	AUP1	LUSC Tumor
cg07727233	1.39E-10	1.448	GSS	LUAD Normal
hsa-mir-4999	0.5929	1.421	MIR4999	LUSC Normal
cg09297514	0.5230	1.395	CAMKK2	LUAD Tumor
ENSG00000138109.9	0.0157	1.378	CYP2C9	LUSC Tumor
ENSG00000099810.17	0.2798	1.365	MTAP	LUSC Normal
cg19273074	0.06963	1.357	PDZRN4	LUSC Normal
ENSG00000134184.11	0.0026	1.301	GSTM1	LUSC Tumor
hsa-mir-138-2	0.03246	1.295	MIR138-2	LUSC Normal
cg19343088	0.7102	1.286	AIM1	LUSC Tumor
cg18441041	0.1053	1.283	CUX1	LUAD Tumor
hsa-mir-181a-2	1.12E-16	1.269	MIR181a-2	LUSC Normal
cg14336879	2.42E-23	1.260	SEZ6,PIPOX	LUAD Tumor
ENSG00000075945.11	0.0014	1.257	KIFAP3	LUSC Normal
ENSG00000117834.11	1.24E-20	1.239	SLC5A9	LUSC Normal
ENSG00000258947.5	0.00020	1.174	TUBB3	LUAD Tumor
hsa-mir-320b-2	7.68E-20	1.166	MIR320b-2	LUSC Tumor
ENSG00000104365.12	0.8046	1.163	IKBKB	LUSC Normal
cg23424800	0.00233	1.161	C8orf74	LUAD Normal
ENSG00000185201.15	6.68E-18	1.158	IFITM2	LUSC Normal
cg08703522	0.1377	1.151	WNT3	LUAD Tumor
ENSG00000136842.12	0.00057	1.134	TMOD1	LUSC Normal
ENSG00000177853.13	0.2412	1.099	ZNF518A	LUSC Normal
ENSG00000100359.19	0.00232	1.070	SGSM3	LUSC Normal
cg18070562	6.01E-20	1.042	ALOXE3	LUAD Normal
cg18575209	3.68E-06	1.022	ZNF586	LUSC Tumor
ENSG00000115896.14	0.000327	1.006	PLCL1	LUSC Normal
ENSG00000022556.14	0.24421	1.002	NLRP2	LUSC Normal
hsa-mir-193a	0.10296	0.989	MIR193a	LUSC Normal
cg12304599	0.19903	0.967	RERG	LUAD Tumor
cg24041269	2.72E-24	0.967	HLTF	LUAD Tumor

miRNA-seq, and important features patterns in LUAD subtype-II compared to LUSC subtype-I lung datasets. Hierarchical clustering organizes cell lines, with labels in purple (subtype-I) and yellow (subtype-II) highlighting LUSC and LUAD patients, respectively. (A) DName, (B) miRNA-seq, (C) RNA-seq, (D) Integrated (A, B, C) omics as Multi-Omic<sub>256</sub> features. (E) Outcome of Top 32 molecular features of integrated Multi-Omic<sub>256</sub> features using QNN<sub>1256</sub> model. We discovered several novel features in DNA-me, miRNA-Seq and RNA-Seq which have a unique diagnostic potential to differentiate LUSC and LUAD subtypes. Fig 8. presents a comparison of QNN models with different encoding features on integrated multi-omic data based on various classification metrics through a boxplot.

Fig (9-10) represents the performance evaluation of the QNN model using various feature sets. Fig 9. depict the visualization of confusion matrices for training datasets with 256, 64, and 32 features, respectively. Similarly, Fig 10. displays confusion matrices for testing datasets with the same feature configurations. Additionally, Fig 9 illustrates the visualization of the Area Under the Curve (AUC-ROC) visualization for the QNN model trained on

256, 64, and 32 features, showcasing performance metrics across training and testing datasets. Table VI presents the performance metrics of QNN models in distinguishing between LUAD and LUSC, using different numbers of features. The table compares precision, recall, F1-score, and accuracy for QNN models trained with 256, 64, and 32 features, respectively. Each metric is reported separately for both LUSC and LUAD classes, demonstrating the model’s ability to classify between these lung dataset subtypes across varying feature dimensions.

### E. Performance of Multi-Omic Model1:QNN-256 and Important Features Identification

MQML-QNN<sub>256</sub> Model achieves superior performance when integrating three modalities while including 915 samples. A Multi-Omic integration final Classification results with all visualizations with a dimension of 256 features shown in Fig. 9. In the integration of QNN<sub>256</sub>, we integrated OMIC<sub>DNA</sub>=85, OMIC<sub>RNA</sub>=86, and OMIC<sub>miRNA</sub>=85 features with 915 sample of subtype-I and subtype-II. Similar parameter metrics results have also been reported that the MQML-QNN<sub>256</sub> model provided slightly better accuracy results in the training dataset than in testing results. As evident from Table VI and Table X, the MQML-QNN<sub>256</sub> provided the best performance for the diagnostic subtype-I and subtype-II Loss= (0.1475 and 0.2527), Accuracy= (0.95 and 0.90), AUC-ROC= (0.94 and 0.96) in training and testing respectively.

### Research Process for Distinguishing LUAD and LUSC Subtypes for QNN<sub>256</sub> model:

We identified the 32 Top-hit features with significant and insignificant features by the proposed MQML-QNN<sub>256</sub> model1: ADH1C, MIR632, MIR3690-1 ECI2, RP3-400B16.4, MIR147b, ZNF788, MIR4442, SMAP2, AUP1, GSS, MIR4999, CAMKK2, CYP2C9, MTAP, PDZRN4, RP11-413B19.2, GSTM1, MIR138-2, MIR3174, AIM1, CUX1, MIR181a-2, SEZ6, PIPOX, KIFAP3, SLC5A9, TUBB3, MIR320b-2, IKBKB, C8orf74, RP1L1, IFITM2, WNT3, TMOD1 and many more. A detailed summary of the information on top-hit features is provided in Table VII. Identification of novel molecular features such as ADH1C, MIR632, and MIR3690-1 is crucial for advancing cancer research, particularly in distinguishing between different subtypes like LUAD and LUSC in lung subtypes. These features, identified through the MQML-QNN<sub>256</sub> model, offer significant insights into disease mechanisms and treatment responses. ADH1C [32] MiR-632 [33] [34] [35], IFITM2 [36], [37] GSTM1, TMOD1 [38], Wnt3 [39], miR-147b [40] [41], miR-4442 [42] PDZRN4 [43], CUX1 [44] [45].

Given a trained MQML-QNN model for classifying lung dataset subtypes (LUAD and LUSC), the most important features for classification can be identified by calculating feature importance scores from model weights and associating features with LUAD or LUSC based on

their mean expression levels.

(i) **Identify Significant Features:** Let  $\{X_i\}$  be the set of features used in the (MQML-LungSC) model for classifying LUAD and LUSC.

(ii) **Compute Feature Importance:** For each feature  $i$ , calculate the feature importance score  $\text{Importance}_i$  as the average of absolute weights:

$$\text{Importance}_i = \frac{1}{n} \sum_{j=1}^n |w_{ij}|$$

where  $w_{ij}$  is the weight for feature  $i$  in instance  $j$ , and  $n$  is the number of instances.

(iii) **Calculate Mean Expression Levels:** Let  $\mu_i^{LUAD}$  and  $\mu_i^{LUSC}$  represent the mean expression levels of feature  $i$  in LUAD and LUSC samples, respectively:

$$\mu_i^{LUAD} = \frac{1}{n_{LUAD}} \sum_{j \in \text{LUAD}} X_{ij}$$

$$\mu_i^{LUSC} = \frac{1}{n_{LUSC}} \sum_{j \in \text{LUSC}} X_{ij}$$

where  $X_{ij}$  is the expression level of feature  $i$  in sample  $j$ , and  $n_{LUAD}$  and  $n_{LUSC}$  are the numbers of LUAD and LUSC samples, respectively.

(iv) **Determine Feature Association:** Classify feature  $i$  based on its mean expression levels:

$$\text{Association}_i = \begin{cases} \text{LUAD} & \text{if } \mu_i^{LUAD} > \mu_i^{LUSC} \\ \text{LUSC} & \text{otherwise} \end{cases}$$

(iv) **Integrate Results:** Combine the feature importance, mean expression levels, and association results into a final table for features identification (BI):

$$\text{BI}_i = (\text{Importance}_i, \mu_i^{LUAD}, \mu_i^{LUSC}, \text{Association}_i)$$

By calculating the feature importance scores and comparing the mean expression levels of features in LUAD and LUSC, we can systematically identify the key features for classifying these subtypes. This thorough analysis allows for a clearer understanding of the differences between LUAD and LUSC, enhancing diagnostic and therapeutic strategies.

## F. Performance of Multi-Omic Model2: QNN-64 and Important Features Identification

In the integration of  $QNN_{64}$ , we integrated  $\text{OMIC}_{DNA}=22$ ,  $\text{OMIC}_{RNA}=21$ , and  $\text{OMIC}_{miRNA}=21$  features with 915 samples of subtype-I and subtype-II. A multi-omic integration final classification results with all visualizations with a dimension of 64 features are shown in Fig. 9-10. The MQML-QNN<sub>64</sub> model provided slightly better accuracy results than MQML-QNN<sub>32</sub> in testing results. As evident from Table VI and Table X, the MQML-QNN<sub>64</sub> provided the best performance for the diagnostic subtype-I and subtype-II Loss= (0.21108 and 0.28467), Accuracy= (0.92 and 0.86), AUC-ROC= (0.97 and 0.92) in training and testing respectively. We identified the 32 Top-hit features with significant and insignificant features by the proposed MQML-QNN<sub>64</sub> model2: TYR, MIR323a, MIR193b, PDIA3, MIR6718, HLTf, HLTf-AS1, MIR1258, HRAS, LRRC56, PRRG3,

TABLE VIII. List of 32 top-hit features and their P-values on using QNN-64 model2.

Feature	Gene Name	P-Value
cg14705695	TYR	0.2329
hsa-mir-323a	MIR323a	8.52E-10
hsa-mir-193b	MIR193b	2.32E-23
ENSG00000167004.11	PDIA3	0.00584
hsa-mir-6718	MIR6718	0.01123
cg02398045	HLTF,HLTFAS1	0.00509
hsa-mir-1258	MIR1258	0.8056
cg25016127	HRAS,LRRC56	0.4157
ENSG00000130032.14	PRRG3	1.48E-23
hsa-mir-3174	MIR3174	0.01899
ENSG00000138109.9	CYP2C9	0.01577
hsa-mir-519a-2	MIR519a-2	0.09878
hsa-mir-6815	MIR6815	0.49621
cg06808983	G6PC3	0.4518
ENSG00000258947.5	TUBB3	0.00020
hsa-mir-552	MIR552	3.86E-21
hsa-mir-182	MIR182	0.0068
ENSG00000177570.12	SAMD12	0.01211
ENSG00000166770.9	ZNF667-AS1	0.4329
cg01025842	FBXL8,TRADD	1.41E-05
ENSG00000114378.15	HYAL1	0.00010
hsa-mir-6868	MIR6868	0.0387
cg21035368	ERCC1	0.7402
ENSG00000143248.11	RGS5	1.85E-19
cg08842508	PABPC1P2	0.2452
ENSG00000169660.14	HEXDC	4.13E-05
cg02665570	LYPLAL1	0.01026
hsa-mir-4685	MIR4685	0.0471
hsa-mir-4665	MIR4665	1.41E-24
cg25208969	ARHGAP23	1.24E-09
cg06676119	PDE1A	0.09512
ENSG00000213949.7	ITGA1	4.22E-23

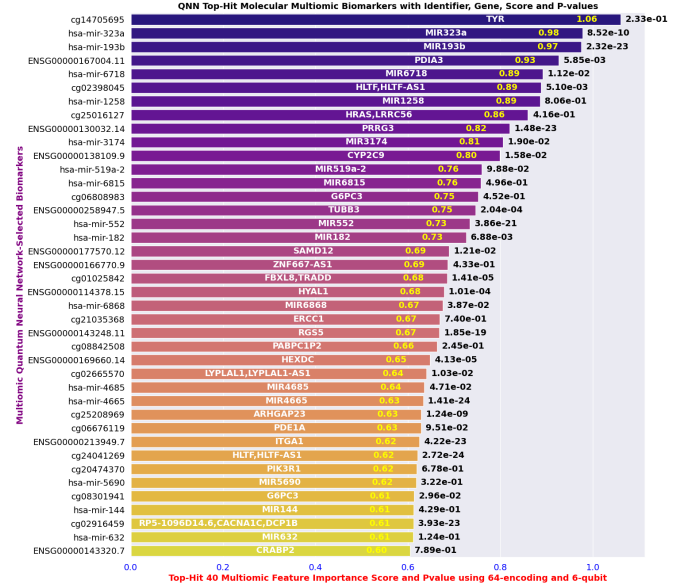


FIG. 11. **Top-Hit Comparison features Visualization of (b) 64 QNN model 2**

MIR3174, CYP2C9, MIR519a-2, MIR6815, G6PC3, TUBB3, MIR552, MIR182, SAMD12, ZNF667-AS1, FBXL8, TRADD, HYAL1, MIR6868, ERCC1, RGS5, PABPC1P2, HEXDC, LYPLAL1, LYPLAL1-AS1, MIR4685, MIR4665, ARHGAP23, PDE1A, ITGA1 and many more. A detailed summary of top-hit features information is provided in Table VIII and Fig 11.

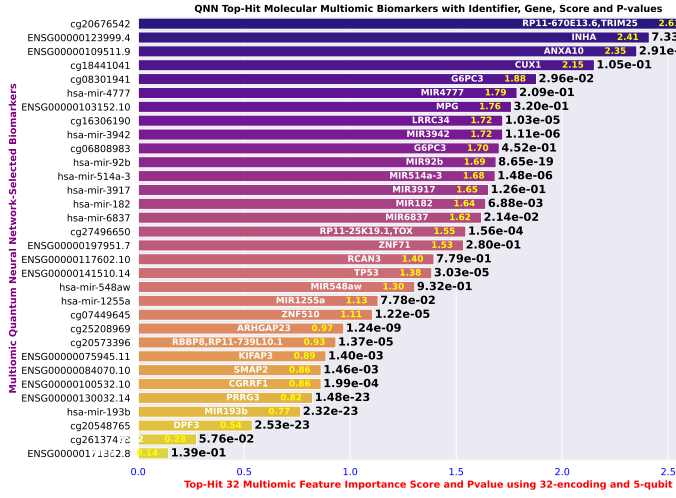


FIG. 12. Top-Hit Comparison features Visualization of (c) 32 of QNN model

TABLE IX. List of 32 top-hit features and their P-values on using QNN-32 model3.

Feature	Gene Name	P-Value
cg20676542	TRIM25	0.4906
ENSG00000123999.4	INHA	0.7333
ENSG00000109511.9	ANXA10	0.00029
cg18441041	CUX1	0.10537
cg08301941	G6PC3	0.02957
hsa-mir-4777	MIR4777	0.2086
ENSG00000103152.10	MPG	0.32002
cg16306190	LRRC34	1.03E-05
hsa-mir-3942	MIR3942	1.11E-06
cg06808983	G6PC3	0.4518
hsa-mir-92b	MIR92b	8.65E-19
hsa-mir-514a-3	MIR514a-3	1.48E-06
hsa-mir-3917	MIR3917	0.12600
hsa-mir-182	MIR182	0.0068
hsa-mir-6837	MIR6837	0.02140
cg27496650	TOX	0.000156
ENSG00000197951.7	ZNF71	0.2799
ENSG00000117602.10	RCAN3	0.7790
ENSG00000141510.14	TP53	3.03E-05
hsa-mir-548aw	MIR548aw	0.9316
hsa-mir-1255a	MIR1255a	0.0777
cg07449645	ZNF510	1.22E-05
cg25208969	ARHGAP23	1.24E-09
cg20573396	RBBP8	1.37E-05
ENSG00000075945.11	KIFAP3	0.00140
ENSG00000084070.10	SMAP2	0.0014
ENSG00000100532.10	CGRRF1	0.0001
ENSG00000130032.14	PRRG3	1.48E-23
hsa-mir-193b	MIR193b	2.32E-23
cg20548765	DPF3	2.53E-23
cg26137478	OSR2	0.0575
ENSG000001171862.8	PTEN	0.1390

### G. Performance of Multi-Omic Model3: QNN-32 and Important Features Identification

A multi-omic integration final classification results with all visualizations with a dimension of 32 features are shown in Fig. 9-10. In the integration of  $QNN_{32}$ , we integrated  $OMIC_{DNA}=11$ ,  $OMIC_{RNA}=10$ , and  $OMIC_{miRNA}=11$  features with 915 sample of subtype-I and subtype-II. The MQML-QNN<sub>32</sub> model provided slightly better confusion matrix subtype clas-

sification i.e. close to  $QNN_{256}$  but slightly better than  $QNN_{64}$  in testing results than training results. As evident from Table X, the MQML-QNN<sub>32</sub> provided the best performance for the diagnostic subtype-I and subtype-II. Loss= (0.21108 and 0.28467), Accuracy= (0.92 and 0.86), AUC-ROC= (0.97 and 0.92) in training and testing respectively. We identified the 32 Top-hit features with significant and insignificant features by the proposed MQML-QNN<sub>32</sub> model3: RP11-670E13.6, TRIM25 INHA, ANXA10, CUX1, G6PC3, MIR4777, MPG, LRRC34, MIR3942, G6PC3, MIR92b, MIR514a-3, MIR3917, MIR182, MIR6837, RP11-25K19.1,TOX, ZNF71, RCAN3, TP53, MIR548aw, MIR1255a, ZNF510, ARHGAP23, RBBP8,RP11-739L10.1, KIFAP3, SMAP2, CGRRF1, PRRG3, MIR193b, DPF3, OSR2, PTEN and many more.

A detailed summary of the information on top-hit features is provided in Table IX and Fig 12. Fig 14 shows the visualization representation with a violin plot, box plot, dot plot, and swarm plot of QNN-256 model top-12 molecular multi-omic features.

### H. Comparison with Classical Machine Learning Models with using Multi-Omic Datasets

In this study, with the aim of enhancing diagnostic lung subtype performance using GDC-TCGA datasets, a novel hybrid-QNN feature selection and diagnostic classification method was first proposed. Subsequently, four machine-learning models were employed to investigate the impact of feature selection methods on classification performance. The classification performance of (MQML-LungSC) was compared to classical classifier algorithms as well as benchmark classification algorithms namely; MLP, SVM, and LR as shown in Fig 13. Training and testing set performance of classical machine learning algorithms and proposed QNN on subtype diagnostic classification. Table X shows that (MQML-LungSC) outperforms all benchmark classification algorithms when trained on different dimensional representations of multiple modalities. This demonstrates the predictive power of the Hybrid Classical QNN learning architecture.

This study compares the performance of our proposed QNN models with classical machine learning models LR, MLP, and SVM—at different dimensions (256, 64, and 32) on a multi-omic dataset. Key metrics include accuracy, loss, and AUC. The performance of QNN models, specifically  $QNN_{256}$ ,  $QNN_{64}$ , and  $QNN_{32}$ , was compared against classical machine learning models such as (LR), (MLP), and (SVM) across different dimensions (256, 64, and 32). The evaluation metrics included Accuracy, Loss, and AUC for both training and testing phases. **Performance of  $QNN_{256}$ :**  $QNN_{256}$  achieved superior performance with a training accuracy of 0.95 and testing accuracy of 0.905. It also outperformed others with a lower loss of 0.1475 during training and 0.2527 during testing. The AUC was notably high at 0.99 for train-

TABLE X. Performance comparison with different classical machine learning models on multi-omic.

Models	Training			Testing		
	Accuracy	Loss	AUC	Accuracy	Loss	AUC
LR <sub>256</sub>	0.748	0.5752	0.9	0.748	0.5869	0.89
LR <sub>64</sub>	0.844	0.5032	0.91	0.797	0.5181	0.89
LR <sub>32</sub>	0.76	0.5112	0.86	0.78	0.5121	0.86
MLP <sub>256</sub>	0.89	0.376	0.96	0.874	0.4101	0.95
MLP <sub>64</sub>	0.78	0.5696	0.88	0.77	0.5787	0.84
MLP <sub>32</sub>	0.75	0.5591	0.82	0.74	0.5715	0.81
SVM <sub>256</sub>	<b>0.93</b>	0.2235	0.96	0.87	0.2658	<b>0.96</b>
SVM <sub>64</sub>	0.88	0.3131	0.93	0.84	<b>0.3545</b>	<b>0.92</b>
SVM <sub>32</sub>	0.83	0.4215	0.89	0.8	0.4704	0.87
QNN <sub>256</sub>	<b>0.95</b>	<b>0.1475</b>	<b>0.99</b>	<b>0.905</b>	<b>0.2527</b>	<b>0.96</b>
QNN <sub>64</sub>	0.92	0.21108	<b>0.97</b>	<b>0.86</b>	0.3849	<b>0.92</b>
QNN <sub>32</sub>	<b>0.88</b>	0.2846	<b>0.95</b>	<b>0.86</b>	<b>0.3863</b>	<b>0.92</b>

ing and 0.96 for testing, indicating excellent classification capability. These metrics indicate that  $QNN_{256}$  not only classifies data with high accuracy but also maintains a low error rate and a high capability to distinguish between classes. Compared to the best classical model,  $SVM_{256}$ , which achieved an accuracy of 0.93, loss of 0.2235, and AUC of 0.96,  $QNN_{256}$  outperforms it in all aspects. This highlights the superiority of QNN in handling complex datasets with greater precision and efficiency.

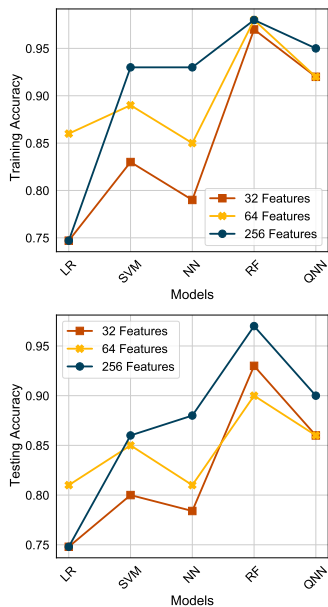


FIG. 13. Training and testing set performance of classical machine learning algorithms and proposed QNN on subtype diagnostic classification.

**Performance of  $QNN_{64}$ :** showed strong performance with a training accuracy of 0.92 and a testing accuracy of 0.86. The training loss was 0.21108, while the testing loss was higher at 0.3849. The AUC values were also competitive, with 0.97 for training and 0.92 for testing. These results are competitive with the  $SVM_{64}$ , which has an accuracy of 0.88, a loss of 0.3131, and an AUC of 0.93. While  $SVM_{64}$  performs well,  $QNN_{64}$  surpasses

it in accuracy and AUC, although the loss is relatively higher. The comparison underscores that  $QNN_{64}$  maintains a significant edge over classical models in terms of classification accuracy and the ability to distinguish between classes.

**Performance of  $QNN_{32}$ :** For the  $QNN_{32}$  model, the performance metrics were still superior to many classical models.  $QNN_{32}$  achieved an with a training accuracy of 0.88 and a testing accuracy of 0.86. The training loss was 0.2846, and the testing loss was 0.3863. The AUC values were 0.95 for training and 0.92 for testing, indicating reliable performance. In comparison, the  $SVM_{32}$  model obtained an accuracy of 0.83, a loss of 0.4215, and an AUC of 0.89. The results indicate that even at a lower dimensional configuration,  $QNN_{32}$  outperforms traditional models, particularly in accuracy and AUC, though the loss metric indicates a slightly higher error rate compared to its higher-dimensional counterparts.

Across all configurations, the QNN consistently outperformed traditional classifiers.  $QNN_{256}$  was the most effective, followed by  $QNN_{64}$  and  $QNN_{32}$ . Traditional models like SVM and MLP showed competitive performance, especially  $SVM_{256}$  with a high AUC of 0.96. However, the logistic regression models consistently lagged behind, with  $LR_{64}$  achieving an accuracy of 0.748, a loss of 0.5752, and an AUC of 0.9, underscoring their limitations in complex data scenarios. The MLP models, while showing reasonable performance, were not able to match the accuracy and AUC of the QNN models, particularly in lower dimensions.

The dimension-wise analysis further reveals the effectiveness of quantum neural networks.  $QNN_{256}$  emerged as the best performer with the highest accuracy (0.95), the lowest loss (0.1475), and the highest AUC (0.99). This model outshined all other models across every metric. Among the 64-dimensional models,  $QNN_{64}$  was superior with an accuracy of 0.92 and an AUC of 0.97, although  $SVM_{64}$  showed a slightly lower loss (0.3131 vs. 0.21108). In the 32-dimensional category,  $QNN_{32}$  led with an accuracy of 0.88 and an AUC of 0.95, proving its robustness even at lower dimensions. These results affirm the potential of QNNs to provide high-performance classification across various dimensions, outperforming classical counterparts consistently.

## V. DISCUSSION

In this paper, we have proposed a (MQML-LungSC)-QNN framework based on quantum neural networks using three different dimensions. With the development of bio-informatics methods, researchers have been able to cover interesting features for LUAD and LUSC, and several relevant papers have been published. To detect biologically relevant markers, numerous studies have aimed to enhance traditional machine-learning algorithms or develop new ones for molecular feature discovery. However, few have employed overlapping machine learning

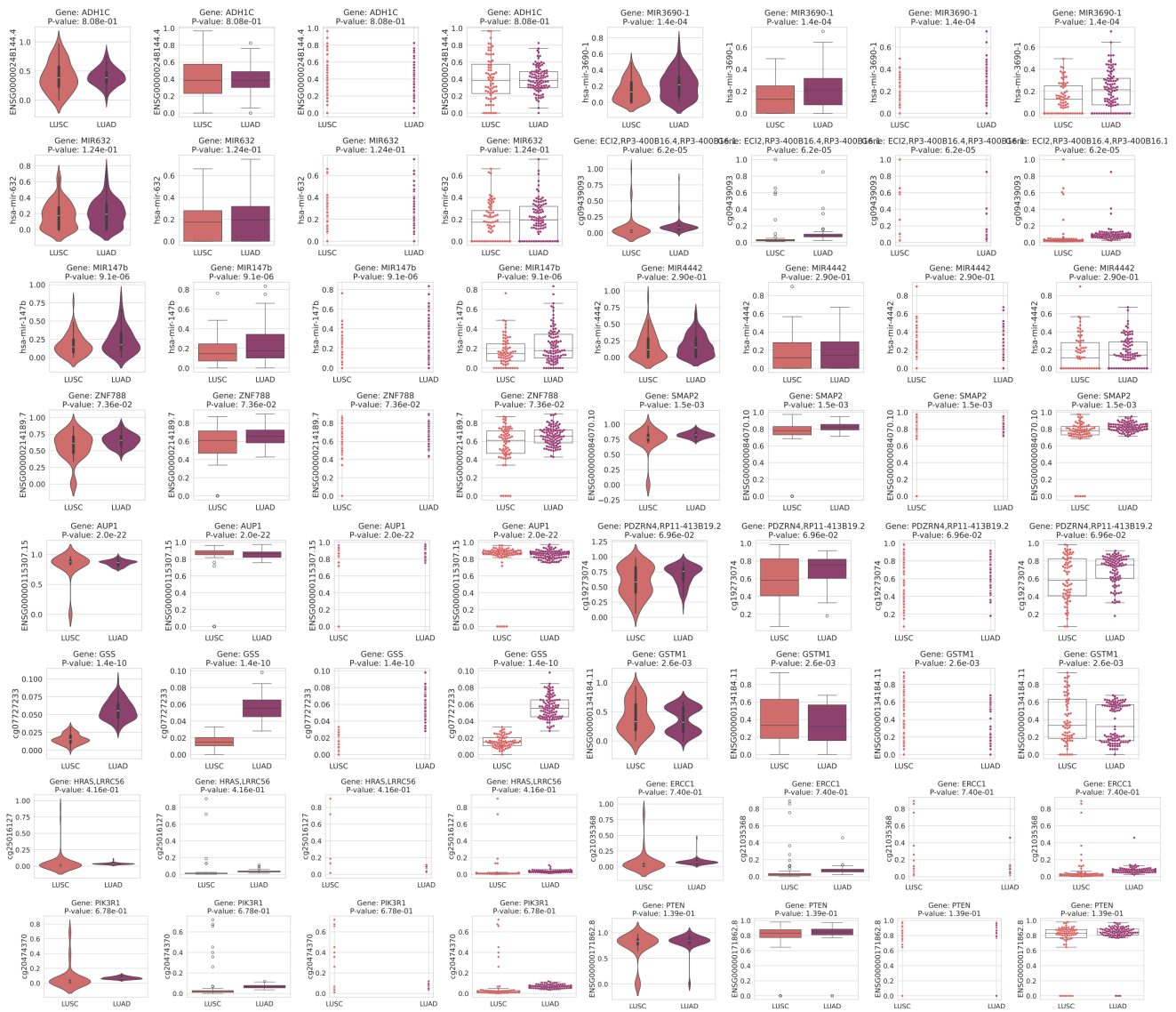
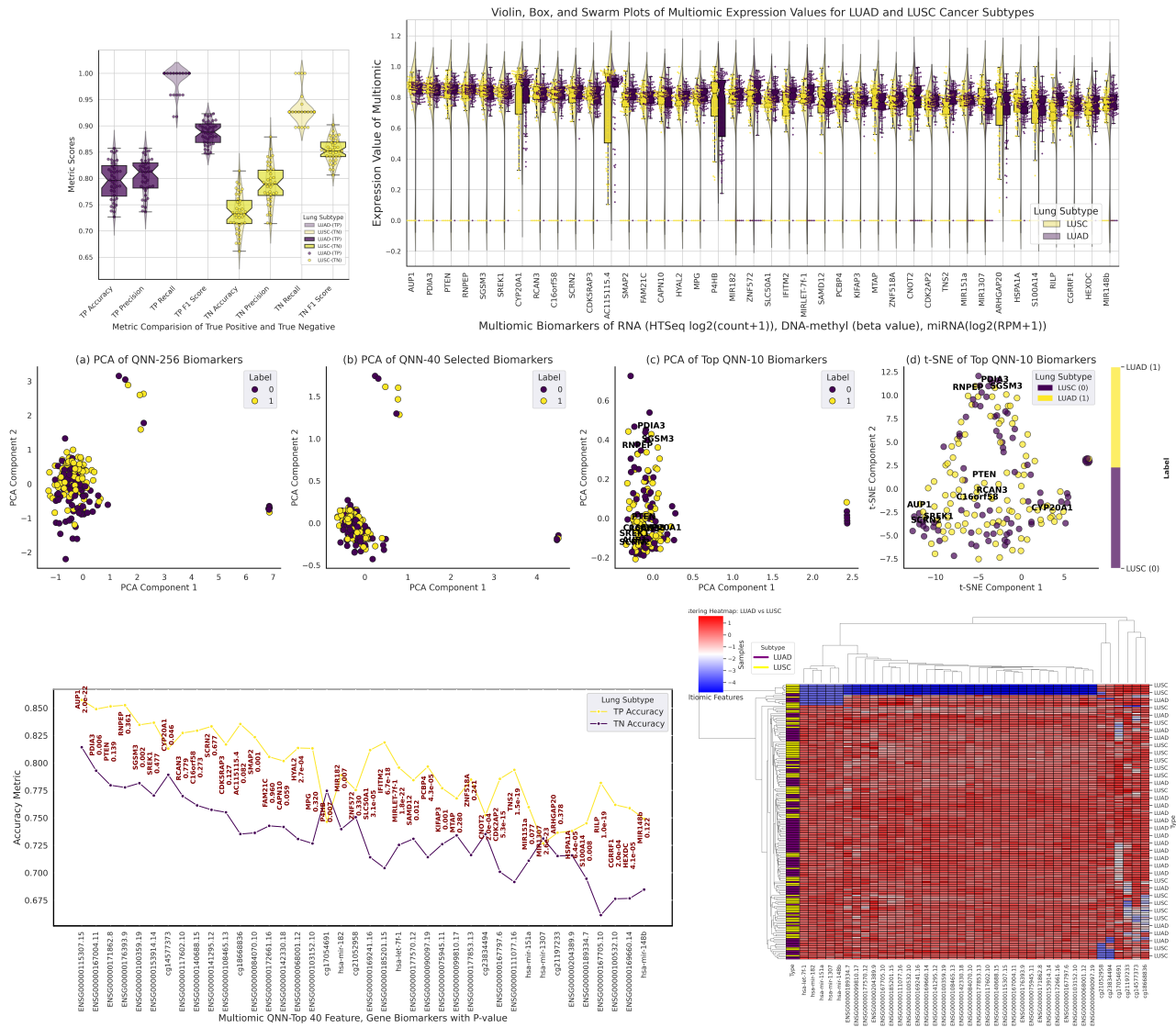


FIG. 14. **Visualization of Multi-Omic-Molecular features** Top-16 hit features visualization representation with a violin plot, box plot, dot plot, and swarm plot of QNN-256 model for diagnostic subtype-I (LUSC) and subtype-II(LUAD) lung classification with identifier name, gene/feature name and P-value

or feature selection methods for cancer classification, best features identification, or gene expression analysis. The author [7] the study proposed using overlapping traditional feature selection for cancer classification and biomarker discovery. The genes selected by the overlapping method were then validated using random forest. Gene expression analysis was subsequently performed to further investigate biological differences between LUAD and LUSC and identified 18 potentially novel features with high discriminating values between LUAD and LUSC. The application of (MQML-LungSC) has been benchmarked on Lung subtype datasets from the GDC-TCGA, namely; LUAD and LUSC. Cancer is widely regarded as a highly heterogeneous disease however, (MQML-LungSC) was able to accurately classify lung dataset sub-types from integrated omic data.

(MQML-LungSC) identified the optimal combination of modalities which resulted in greater patient coverage while maintaining a state-of-the-art classification performance compared to its different dimensions of features as shown in Fig 4-5-6-7. We identified the top 32 features from model 1  $QNN_{256}$  features, another top 32 features from model 2  $QNN_{64}$  features, and the top 32 features from model 3  $QNN_{32}$  features using feature selection method and QNN diagnostic classifier that have potential to differentiate the subtype-I and subtype-II. In comparing the performance of our proposed models,  $QNN_{256}$ ,  $QNN_{64}$ , and  $QNN_{32}$ , it is evident that  $QNN_{256}$  exhibits superior results across several metrics both in training and testing phases. Overall, the QNN models, particularly  $QNN_{256}$ , outperformed the classical models across most evaluation metrics.  $QNN_{256}$  demon-



**FIG. 15. Visualization of Multi-omic Molecular features with  $QNN_{256}$  Predictions** Left Side: First row depicts the metric performance comparison of (LUAD)-TP and (LUSC)-TN, Right side: Visualization representation of 40 features via Violin, Box, and Swarm plots of Multi-omic expression values for LUAD and LUSC subtypes. In the Second Row: (a) Pca representation of  $QNN_{256}$  model with 256 features before predictions, (b) After selecting 40-features for  $QNN_{256}$  with PCA, (c) After selecting the top-best representation of 10-features for  $QNN_{256}$  with PCA and (d) TSNE representation that separated the LUAD and LUSC group of subtypes very well.

strated the highest accuracy, lowest loss, and superior AUC, making it the most robust model in this comparison.  $QNN_{64}$  and  $QNN_{32}$  also showed strong results, particularly in terms of AUC, validating the effectiveness of quantum neural networks for multi-omic data classification tasks.

### A. Simulation Analysis on $QNN_{256}$ Model to Find the Best Features Based on Performance Metrics

In this study, we aimed to identify key features (genes) that contribute to the accurate classification of lung

dataset subtypes (LUAD and LUSC). With the help of  $QNN_{256}$  model, we employed a comprehensive approach to identifying the top 40 best features from multi-omic data by leveraging performance metrics of a predictive model. The process began by predicting test samples and evaluating the model's performance using a confusion matrix, from which we derived key metrics such as accuracy, precision, recall, and F1-score for true positive (TP) and true negative (TN) cases. We then calculated the mean feature values for TP and TN samples, followed by deviations from the overall mean. We computed aggregate scores by normalizing and combining TP and TN metrics to rank features. This led to identify-

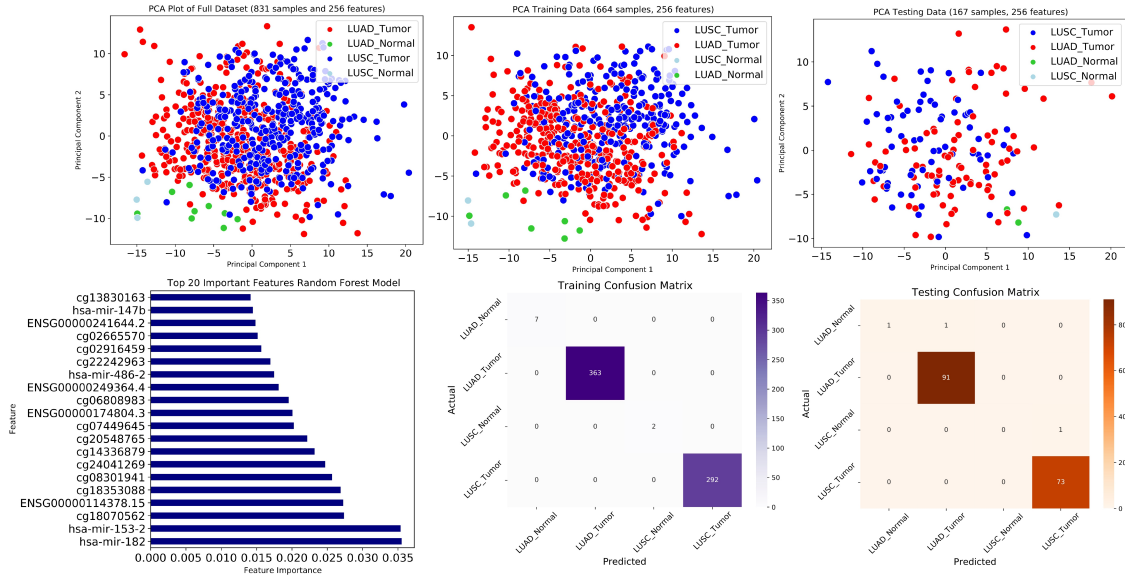


FIG. 16. Visualization of 256-feature classification using a Random Forest model on multi-omic molecular features ( $ML_{256}$  predictions). Top section: (a) The first row shows a PCA plot of the 256 features, displaying the training and testing datasets. (b) The second row presents the confusion matrix for both the training and testing datasets. (c) Bottom section: A visualization of the 20 best features identified by the Random Forest model, distinguishing between LUAD-tumor, LUAD-normal, LUSC-tumor, and LUSC-normal subtypes.

TABLE XI. List of 21 top-hit features and their P-values on using QNN-256 and RF model analysis

Identifier Names	Gene	Pvalue	Feature-specific	FI	Outcome
ENSG00000140688.15	C16orf58	0.2731	LUAD-Tumor	0.1029	Less Significant
ENSG00000108465.13	CDK5RAP3	0.12661	LUAD-Tumor	0.1369	Less Significant
ENSG00000103152.10	MPG	0.3200	LUAD-Tumor	0.039	Less Significant
cg21052958	ZNF572	0.330273	LUAD-Tumor	0.1258	Less Significant
hsa-mir-151a	MIR151a	0.07682	LUAD-Tumor	0.097	Less Significant
hsa-mir-148b	MIR148b	0.12183	LUAD-Tumor	0.1413	Less Significant
hsa-mir-153-2	MIR153-2	0.1332	LUAD-Tumor	0.09582	Less Significant
ENSG00000142330.18	CAPN10	0.05855	LUAD-Tumor	0.1578	Most Significant
ENSG00000169241.16	SLC50A1	3.07E-05	LUAD-Tumor	0.0363	Most Significant
ENSG00000169660.14	HEXDC	4.13E-05	LUAD-Tumor	0.137	Most Significant
hsa-mir-147b	MIR147b	9.10E-06	LUAD-Tumor	1.51868	Most Significant
ENSG00000257842.4	NOVA1-AS1	0.0378	LUAD-Tumor	0.11304	Most Significant
ENSG00000132744.6	ACY3	5.57E-24	LUAD-Tumor	0.15902	Most Significant
hsa-mir-182	MIR182	0.00688	LUSC-Tumor	0.09	Most Significant
ENSG00000204389.9	HSPA1A	6.38E-05	LUSC-Tumor	0.0848	Most Significant
ENSG00000189334.7	S100A14	0.0077	LUSC-Tumor	0.10036	Most Significant
ENSG00000134184.11	GSTM1	0.00261	LUSC Tumor	1.3014	Most Significant
ENSG00000171862.8	PTEN	0.13904	LUSC Tumor	0.88	Less Significant
cg21035368	ERCC1	0.740247569	LUSC Tumor	0.67	Less Significant
cg20474370	PIK3R1	0.678445797	LUSC Tumor	0.62	Less Significant
cg25016127	HRAS	0.415771079	LUSC Tumor	0.86	Less Significant

ing the top features with the highest deviations and best performance metrics. The final selection of the top 40 features was based on these aggregate scores, providing a robust set of best features for further analysis. This methodology ensures a balanced consideration of feature performance in distinguishing between LUAD and LUSC labels. Fig 15. illustrates the results of  $QNN_{256}$  predictions on multi-omic-molecular features. The left side displays a performance comparison between LUAD-TP and LUSC-TN metrics, while the right side shows the visualization of 40 important features through violin, box, and swarm plots for LUAD and LUSC subtypes. The second row includes: (a) PCA representation of  $QNN_{256}$  with

256 features before predictions; (b) PCA after selecting 40 features; (c) PCA with the top 10 features; and (d) t-SNE representation effectively separating LUAD and LUSC subtypes. In this analysis 40 features genes along with their performance metrics in distinguishing between LUAD (True Positive) and LUSC (True Negative) cases. Each gene is evaluated based on its p-value, accuracy, precision, recall, and F1-score for LUAD and LUSC classifications. This comprehensive overview highlights the effectiveness of each features, with emphasis on those showing both high statistical significance and strong classification performance, providing valuable insights into their potential utility in cancer diagnostics. Table XI

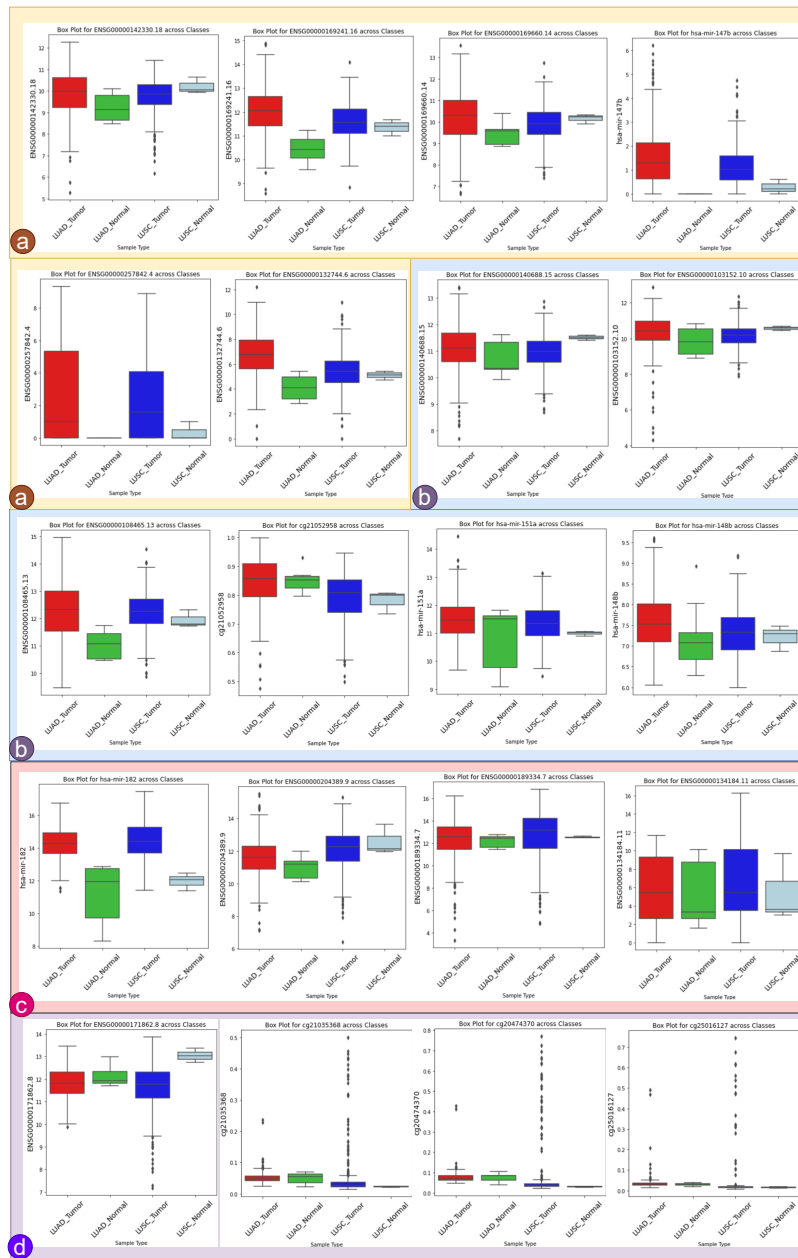


FIG. 17. Visualization of 21 out of 256 most and least significant genes based on p-values for LUAD and LUSC cohorts, distinguishing between tumor and normal samples. (a) depicts the most significant LUAD-specific genes with a yellow outline, (b) depicts the least significant LUAD-specific genes with a blue outline, and (c) depicts the most significant LUSC-specific genes with a pink outline, (d) depicts the less significant LUSC-specific genes with a purple outline. Box plots show multiomic level values for LUAD-tumor, LUAD-normal, LUSC-tumor, and LUSC-normal subtypes.

presents based on the above  $QNN_{256}$  analysis and random forest (RF) model analysis, a total of 21 biomarkers were identified for LUAD and LUSC tumors. Among them, 7 biomarkers were found to be less significant in LUAD tumors, while 6 biomarkers were classified as most significant for LUAD. For LUSC tumors, 4 biomarkers were identified as most significant and 4 biomarkers were identified as less significant. This distribution under-

scores the differing levels of biomarker relevance in LUAD and LUSC, suggesting potential targets for further investigation in both cancer types. In the LUAD dataset, the most significant genes include SLC50A1 (p-value =  $3.07E-05$ ), HEXDC (p-value =  $4.13E-05$ ), MIR147b (p-value =  $9.10E-06$ ), and ACY3 (p-value =  $5.57E-24$ ), all of which exhibit strong associations with LUAD tumors. On the other hand, less significant genes in LUAD include

C16orf58 (p-value = 0.2731), CDK5RAP3 (p-value = 0.12661), and MPG (p-value = 0.320029). In the LUSC dataset, significant genes such as MIR182 (p-value = 0.00688) and GSTM1 (p-value = 0.002615542) stand out, while genes like PTEN (p-value = 0.13904) and ERCC1 (p-value = 0.740247569) are among the less significant. In Fig. 16, the analysis involved combining RNA, DNA, and miRNA data, resulting in a dataset of 831 samples and 256 (selected features). Labels for the sample types (LUAD and LUSC, tumor and normal) were encoded into numeric classes for model training. Before applying machine learning, PCA was performed to visualize the variance in the dataset. The data was then split into training (80%) and testing (20%) sets, with 664 samples used for training and 167 for testing. A Random Forest classifier was trained using class-balanced weights, yielding a high testing accuracy of 98.8%. The model performed well for LUAD and LUSC tumor classes, but had difficulty with LUSC normal due to the small sample size, reflected in zero recall for that class. Feature importance analysis revealed the top 20 most significant features, which were visualized. Multiple plots, including PCA scatter plots, confusion matrices, and box plots, were generated to assess model performance and the distribution of key features across the sample types.

### B. Model Compilation Parameters

In this paper, we have created the function `MetricsCallback` to evaluate the performance of a machine learning model during training. The evaluation metrics include accuracy, precision, recall, and F1-score. These metrics are widely used in classification tasks to assess the model’s ability to classify instances belonging to different classes correctly. All methods use the Adaptive Moment Estimation (Adam) optimizer; the learning rate is set to 0.01, and the batch size is 16. The experiments are conducted using the PennyLane quantum programming framework (version 0.28.0) in Python 2.8.0. The details of the classification metrics are given

**Accuracy:** It is used to evaluate how often the predictions match the actual labels and defined as the ratio of correctly predicted instances to the total instances:

$$\text{Accuracy} = \frac{1}{N} \sum_{i=1}^N \mathbf{1}(\hat{y}_i = y_i) \quad (20)$$

where  $\mathbf{1}(\cdot)$  is the indicator function that returns 1 if the condition inside is true and 0 otherwise.

**Precision Score:** It is defined as the ratio of true positive predictions to the total number of positive predictions made by the model as

$$\text{Precision} = \frac{\sum_{i=1}^N TP_i}{\sum_{i=1}^N (TP_i + FP_i)} \quad (21)$$

where  $TP_i$  represents the number of true positive predictions for class  $i$  and  $FP_i$  represents the number of false positive predictions for class  $i$ .

**Recall Score:** It is also known as sensitivity, and measures the ability of the model to correctly identify positive instances out of all actual positive instances. Mathematically, it is represented as:

$$\text{Recall} = \frac{\sum_{i=1}^N TP_i}{\sum_{i=1}^N (TP_i + FN_i)} \quad (22)$$

where  $FN_i$  represents the number of false negative predictions for class  $i$ .

**F1-score:** It is the harmonic mean of precision and recall, providing a balance between the two metrics. It is calculated using the formula:

$$F_1 = 2 \times \frac{\text{Precision} \times \text{Recall}}{\text{Precision} + \text{Recall}} \quad (23)$$

## VI. CONCLUSION

To the best of our knowledge, this study is the first to investigate the difference between LUSC and LUAD using the GDC-TCGA data within a hybrid classical-quantum classification model. In the classical part of the study, a feature selection method was used to determine the best and unique subset of multi-omic molecular features using the GDC-TCGA dataset. The proposed model involves applying a QNN with classical dense layers for diagnosing lung subtype-I and subtype-II. This model’s performance was compared with various classical machine learning classifiers, including Logistic Regression, Support Vector Machine, and Random Forest. Bench-marking with Quantum neural network ( $QNN_{256}$ ), and the comparison included all existing models using 256, 64 and 32 features of integrated multi-omics data. The empirical results demonstrate that Quantum Neural Networks, particularly  $QNN_{256}$ , offer significant improvements over classical machine learning models. The superior performance in terms of accuracy, loss, and AUC suggests that QNNs are highly effective in handling complex data and providing accurate classifications. The  $QNN_{256}$  model, with its exceptional metrics, stands out as the most promising, indicating the potential of quantum-based approaches to revolutionize machine learning. The overall comparison highlights the potential of quantum machine learning to surpass traditional methods, providing a compelling case for further exploration and development in this field. The dimension-wise analysis reaffirms the robustness and efficacy of QNNs, particularly at higher dimensions, where they consistently outperform classical models across all metrics. We employed two approaches to identify best features. First, we trained  $QNN_{256}$ ,  $QNN_{64}$ , and  $QNN_{32}$  models separately and determined the top 32 features for each model based on the QNN model weights. Also, we visualized the top-12 hit features using various plots. This included violin, box, dot, and

swarm plots from the  $QNN_{256}$  model for diagnostic classification of lung subtypes (LUSC and LUAD). Each plot displayed the identifier name, gene/feature name, and P-value for effective comparison. In the second approach, the  $QNN_{256}$  model was used to predict labels for 183 test samples, followed by evaluation using confusion matrices to derive key metrics like accuracy, precision, recall, and F1-score for true positive (TP) and true negative (TN) cases. We calculated mean feature values and deviations for TP and TN samples, then ranked features based on normalized aggregate scores. The top 40 features were selected from these scores, ensuring a comprehensive assessment of feature performance for distinguishing LUAD and LUSC subtypes. In this research, we distinguished between LUAD and LUSC subtypes by integrating feature importance with mean expression levels. First, we extracted feature importance from the model by averaging the absolute weights of each feature. Next, we calculated the mean expression levels of features in LUAD and LUSC samples using the equations.

**In the future**, we aim to enhance our work by focusing on deeper biological insights as well as quantum. In **Phase 1**, we will identify LUAD-specific and LUSC-specific genes by first applying a p-value t-test between tumor and normal samples, followed by differential analysis to further distinguish LUAD-specific genes and LUSC-specific genes. This will help identify additional biomarkers with potential prognostic value for cancer-specific between two subtypes. **Phase 2** will involve developing a quantum classifier to distinguish between tumor and normal samples, as well as between LUAD type-1 and LUSC type-2 tumors. This will classify the four sample groups and identify the top hit biomarkers specific to each cancer subtype. This approach will also highlight the significant p-values for LUAD- and LUSC-specific genes, enabling a clearer distinction between the two cancer types. Additionally, we will demonstrate the quantum advantage in a biologically meaningful context. Also, we plan to use these biomarkers for survival analysis to identify high-risk and low-risk clinical patients. We will also explore biological implications through Gene Ontology (GO) analysis and Kaplan-Meier survival curves. Additionally, we aim to compare correlations between classical and quantum analysis methods to understand their effectiveness in cancer research.

#### Data availability

All data generated and/or analyzed during the current study are included in this article. The data in this paper were obtained from The Can-

cer Genome Atlas (GDC-TCGA) Research Network. <https://www.cancer.gov/tcga>) The underlying code for this study is not publicly available but may be made available to qualified researchers on reasonable request from the corresponding author.

Single Omics: (1) DNA-Methylation (2) MicroRNA-seq (3) RNA-seq Source name and link: UCSC XENA GDC-TCGA Dataset UCSC Xena: GDC Xena Hub. The hub hosts v18.0 release from the GDC Data Portal.

Open and Select OMICs for Download: Github Link download: <https://xenabrowser.net/datapages/>

(1) DNA: Illumina Human Methylation 450 (n=503) GDC Hub, unit= beta value Download: (2) miRNA-seq: stem-loop expression miRNA Expression Quantification (n=564) GDC Hub, unit=  $\log_2(\text{RPM}+1)$  (3) RNA-seq: gene expression RNAseq, HTSeq - Counts (n=585) GDC Hub, unit=  $\log_2(\text{count}+1)$  (4) Phenotype and clinical data Download Phenotype clinical: TCGA-LUAD GDC phenotype Download Survival data: TCGA-LUAD survival

#### CONFLICT OF INTEREST

The authors declare that they have no conflicts of interest.

#### ACKNOWLEDGEMENTS

We would like to acknowledge the financial support of Purdue Quantum Science and Engineering Institute and U.S. Department of Energy (Office of Basic Energy Sciences) under Award No. DE-SC0019215.

#### AUTHOR CONTRIBUTIONS

S.K. and H.G. conceived and supervised the project. M.K.S and A.S.B. designed the framework, and performed the simulations. M.K.S. wrote the initial manuscript and contributed to the development and visualization. The Data feature engineering phase was conducted by M.I. and M.K.S. Resources and Funding acquisition by S.K. All authors contributed to analyzing the results and finalizing the manuscript.

#### DATA AND SOFTWARE AVAILABILITY

The authors confirm that the data supporting the findings of this study are available from the corresponding author, upon reasonable request.

---

[1] P. Board, Non-small cell lung cancer treatment (pdq), PDQ Cancer Information Summaries [Internet] (2024).

[2] J. Biamonte, P. Wittek, N. Pancotti, P. Rebentrost, N. Wiebe, and S. Lloyd, Quantum machine learning, Na-

- ture **549**, 195 (2017).
- [3] D. Ristè, M. P. D. Silva, C. A. Ryan, A. W. Cross, A. D. Córcoles, J. A. Smolin, J. M. Gambetta, J. M. Chow, and B. R. Johnson, Demonstration of quantum advantage in machine learning, *npj Quantum Information* **3**, 16 (2017).
  - [4] A. S. Bhatia, M. K. Saggi, and S. Kais, Quantum machine learning predicting adme-tox properties in drug discovery, *Journal of Chemical Information and Modeling* **63**, 6476 (2023).
  - [5] A. S. Bhatia, S. Kais, and M. A. Alam, Federated quantum machine learning: a new paradigm for collaborative quantum learning, *Quantum Science and Technology* **8**, 045032 (2023).
  - [6] A. S. Bhatia, S. Kais, and M. Alam, Handling privacy-sensitive clinical data with federated quantum machine learning, in *APS March Meeting Abstracts*, Vol. 2023 (2023) pp. T70–007.
  - [7] K. Prousalis and N. Konofaos, A quantum pattern recognition method for improving pairwise sequence alignment, *Scientific reports* **9**, 7226 (2019).
  - [8] A. S. Boev, A. S. Rakitko, S. R. Usmanov, A. N. Kobzeva, I. V. Popov, V. V. Ilinsky, E. O. Kiktenko, and A. K. Fedorov, Genome assembly using quantum and quantum-inspired annealing, *Scientific Reports* **11**, 13183 (2021).
  - [9] E. H. Houssein, Z. Abohashima, M. Elhoseny, and W. M. Mohamed, Hybrid quantum-classical convolutional neural network model for covid-19 prediction using chest x-ray images, *Journal of Computational Design and Engineering* **9**, 343 (2022).
  - [10] A. S. Bhatia, M. K. Saggi, A. Kumar, and S. Jain, Matrix product state-based quantum classifier, *Neural computation* **31**, 1499 (2019).
  - [11] R. Xia and S. Kais, Quantum machine learning for electronic structure calculations, *Nature Communications* **9**, 4195 (2018).
  - [12] J. Biamonte, P. Wittek, N. Pancotti, P. Rebentrost, N. Wiebe, and S. Lloyd, Quantum machine learning, *Nature* **549**, 195 (2017).
  - [13] M. Sajjan, S. H. Sureshbabu, and S. Kais, Quantum machine-learning for eigenstate filtration in two-dimensional materials, *Journal of the American Chemical Society* **143**, 18426 (2021).
  - [14] M. Sajjan, J. Li, R. Selvarajan, S. H. Sureshbabu, S. S. Kale, R. Gupta, V. Singh, and S. Kais, Quantum machine learning for chemistry and physics, *Chemical Society Reviews* **51**, 6475 (2022).
  - [15] E. Akpinar and M. Oduncuoglu, Beyond limits: Charting new horizons in glioma tumor classification through hybrid quantum computing with the cancer genome atlas (tcga) data, in press (2024).
  - [16] J. W. Chen and J. Dhahbi, Lung adenocarcinoma and lung squamous cell carcinoma cancer classification, biomarker identification, and gene expression analysis using overlapping feature selection methods, *Scientific reports* **11**, 13323 (2021).
  - [17] M. Esteller, Cancer epigenomics: Dna methylomes and histone-modification maps, *Nature Reviews Genetics* **8**, 286 (2007).
  - [18] C. Network and Others, Comprehensive genomic characterization of squamous cell lung cancers, *Nature* **489**, 519 (2012).
  - [19] V. Relli, M. Trerotola, E. Guerra, and S. Alberti, Abandoning the notion of non-small cell lung cancer, *Trends In Molecular Medicine* **25**, 585 (2019).
  - [20] Z. Huang, L. Chen, and C. Wang, Classifying lung adenocarcinoma and squamous cell carcinoma using rna-seq data, *Cancer Stud Mol Med Open J* **3**, 27 (2017).
  - [21] Z. Cai, D. Xu, Q. Zhang, J. Zhang, S. M. Ngai, and J. Shao, Classification of lung cancer using ensemble-based feature selection and machine learning methods, *Molecular BioSystems* **11**, 791 (2015).
  - [22] X. Y. Liu, S. B. Wu, W. Q. Zeng, Z. J. Yuan, and H. B. Xu, Logsum+ l<sub>2</sub> penalized logistic regression model for biomarker selection and cancer classification, *Scientific reports* **10**, 22125 (2020).
  - [23] W. Li, Mutual information functions versus correlation functions, *Journal of Statistical Physics* **60**, 823 (1990).
  - [24] Y. Yang and J. O. Pedersen, A comparative study on feature selection in text categorization, in *ICML*, Vol. 97 (1997) pp. 412–420.
  - [25] L. Breiman, Random forests, *Machine Learning* **45**, 5 (2001).
  - [26] I. T. Jolliffe, *Principal component analysis for special types of data* (Springer, 2002).
  - [27] D. Müllner, Modern hierarchical, agglomerative clustering algorithms, arXiv preprint arXiv:1109.2378 (2011).
  - [28] T. Hastie, R. Tibshirani, and J. H. Friedman, *The elements of statistical learning: data mining, inference, and prediction*, Vol. 2 (Springer, 2009).
  - [29] K. D. Toennies, 7 multi-layer perceptron for image classification, in *An Introduction to Image Classification: From Designed Models to End-to-End Learning* (Springer, 2024) pp. 139–167.
  - [30] V. Vapnik, *The nature of statistical learning theory* (Springer Science & Business Media, 2013).
  - [31] P. University, Gilbreth high-performance computing cluster (2023), [Accessed: Jan. 2023].
  - [32] V. Bagnardi, M. Rota, E. Botteri, L. Scotti, M. Jenab, R. Bellocco, I. Tramacere, C. Pelucchi, E. Negri, C. L. Vecchia, *et al.*, Alcohol consumption and lung cancer risk in never smokers: a meta-analysis, *Annals of oncology* **22**, 2631 (2011).
  - [33] J. Pu, J. Wang, Z. Xu, Y. Lu, X. Wu, Y. Wu, Z. Shao, and Q. Tang, mir-632 functions as oncogene in hepatocellular carcinoma via targeting myct1, *Human Gene Therapy Clinical Development* **30**, 67 (2019).
  - [34] Z. Z. Zhou, Z. P. Zhang, Z. T. Tao, and T. T. Zhao, mir-632 promotes laryngeal carcinoma cell proliferation, migration, and invasion through negative regulation of gsk3 $\beta$ , *Oncology Research* **28**, 21 (2020).
  - [35] A. Mitra, J. W. Rostas, D. L. Dyess, L. A. Shevde, and R. S. Samant, Micro-rna-632 downregulates dnaib6 in breast cancer, *Laboratory Investigation* **92**, 1310 (2012).
  - [36] Y. Liu, X. Li, J. Huang, J. Huang, Q. Zhu, J. Wang, and M. Luo, High expression of iftm2 in gastric cancer is related to poor prognosis, in press (2022).
  - [37] C. A. Acevedo, L. A. Quiñones, J. Catalán, D. D. Cáceres, J. A. Fullá, and A. M. Roco, Impact of cyp1a1, gstm1, and gstm1 polymorphisms in overall and specific prostate cancer survival, *Urologic Oncology: Seminars and Original Investigations* **32**, 280 (2014).
  - [38] T. Guo, H. Ma, and Y. Zhou, Bioinformatics analysis of microarray data to identify the candidate biomarkers of lung adenocarcinoma, *PeerJ* **7**, e7313 (2019).

- [39] N. Nakashima, D. Liu, C. Huang, M. Ueno, X. Zhang, and H. Yokomise, Wnt3 gene expression promotes tumor progression in non-small cell lung cancer, *Lung Cancer* **76**, 228 (2012).
- [40] L. Yi, X. Zhong, Z. Chen, Q. Wang, Y. Yan, J. Wang, and X. Deng, MicroRNA-147b promotes proliferation and invasion of human colorectal cancer by targeting ras oncogene family (rap2b), *Pathobiology* **86**, 173 (2019).
- [41] D. Ke, Q. Guo, T. Y. Fan, and X. Xiao, Analysis of the role and regulation mechanism of hsa-mir-147b in lung squamous cell carcinoma based on the cancer genome atlas database, *Cancer Biotherapy & Radiopharmaceuticals* **36**, 280 (2021).
- [42] J. Shibamoto, T. Arita, H. Konishi, S. Kataoka, H. Furuke, W. Takaki, J. Kiuchi, H. Shimizu, Y. Yamamoto, and S. Komatsu, Roles of mir-4442 in colorectal cancer: Predicting early recurrence and regulating epithelial-mesenchymal transition, *Genes* **14**, 1414 (2023).
- [43] P. Jin, L. Wu, G. Zhang, B. Yang, and B. Zhu, Pdzrn4 suppresses tumorigenesis and androgen therapy-resistance in prostate cancer, *Journal of Cancer* **13**, 2293 (2022).
- [44] X. Wu, F. Feng, C. Yang, M. Zhang, Y. Cheng, Y. Zhao, Y. Wang, F. Che, J. Zhang, and X. Heng, Upregulated expression of cux1 correlates with poor prognosis in glioma patients: a bioinformatic analysis, *Journal of Molecular Neuroscience* **69**, 527 (2019).
- [45] S. A. El-Aarag, A. Mahmoud, M. H. Hashem, H. A. Elkader, A. E. Hemeida, and M. ElHefnawi, In silico identification of potential key regulatory factors in smoking-induced lung cancer, *BMC Medical Genomics* **10**, 1 (2017).